Position-sensitive germanium detectors for γ-ray tracking, imaging and polarimetry

ANTON KHAPLANOV

Doctoral Thesis in Physics
Stockholm, Sweden 2010

TRITA-FYS 2010:04
ISSN 0280-316X
ISRN KTH/FYS/–10:04–SE
ISBN 978-91-7415-555-6

KTH Physics
SE-106 91 Stockholm
SWEDEN

Akademisk avhandling som med tillstånd av Kungl Tekniska högskolan framlägges till offentlig granskning för avläggande av teknologie doktorsexamen i fysik fredagen den 26 februari 2010 klockan 10.00 i sal FB54, AlbaNova Universitetscentrum, Stockholm.

Tryck: Universitetsservice US-AB

Abstract

Modern germanium detectors are often manufactured with two-dimensionally segmented electrical contacts. Signals induced in each segment are read out simultaneously when a photon is detected. Detailed pulse shape analysis (PSA) of these signals allows to resolve positions of individual γ-ray interactions with a precision of at least a few mm. The track of a photon can then be reconstructed using γ-ray tracking. Using these techniques, highly efficient large-volume germanium detectors can replace detector systems where previously highly granulated detector arrays were required, and/or large fractions of photons had to be rejected. The ability to reconstruct the direction of an incoming photon and its scattering path makes it possible to use segmented detectors for γ-ray imaging and polarimetry. Doppler correction of photon energies in experiments where γ rays are emitted from fast ion beams can be greatly improved due to improved determination of the emission angle with respect to the beam. Furthermore, arrays of many detectors can be built without the need for conventional anticoincidence detectors for escape suppression. Instead, photons escaping a detector crystal can be tracked through neighbouring ones.

In this work position reconstruction accuracy was evaluated for segmented detectors in a number of geometries in realistic applications. Particular emphasis has been put on the reconstruction of data sets containing events of arbitrary complexity in terms of the number of hit segments and interactions per segment. The imaging and polarization sensitivities of a single planar germanium pixel detector have been evaluated experimentally. In these measurements, photons absorbed in two, often adjacent, segments were reconstructed. Simulated interactions of γ-rays with the detectors of the proposed DESPEC germanium array were analysed yielding the position resolution obtainable in realistic experimental situations, as well as its dependence on photon energy, event complexity, noise and other sources of error.

Contents

List of Papers

This thesis is based on the following papers.

1. A. Khaplanov, J. Pettersson, B. Cederwall, *Compton imager based on a single planar segmented HPGe detector*, Nucl. Instr. and Meth. A580 (2007), 1075.

2. A. Khaplanov, S. Tashenov, B. Cederwall, G. Jaworski, *A gamma-ray polarimeter based on a single segmented planar HPGe detector*, Nucl. Instr. and Meth. A593 (2008), 459.

3. A. Khaplanov, B. Cederwall, S. Tashenov, *Position sensitivity of segmented planar HPGe detectors for the DESPEC project at FAIR*, Nucl. Instr. and Meth. A592 (2008), 325.

4. A. Khaplanov, S. Tashenov, B. Cederwall, *Position sensitivity of the proposed segmented germanium detectors for the DESPEC project*, Nucl. Instr. and Meth. A604 (2009), 56.

The author performed most of the work contributing to the above papers. Major contributions by others include the following. The image reconstruction as well as the Monte Carlo simulation for the experiment in paper 1 were done by J. Pettersson. The analysis of data for paper 2 was performed in collaboration with S. Tashenov. In the third paper, the Monte Carlo simulation of the interactions of photons with the detector were performed by S. Tashenov. The fourth paper details the author's contribution to the collaborative work further described in paper 6 below. Papers 5 and 6 include minor contributions by the author, however, are closely related to the thesis.

5. S. Tashenov, A. Khaplanov, B. Cederwall, K.-U. Schässburger, *Hard X-ray polarimetry by means of Rayleigh scattering*, Nucl. Instr. and Meth. A600 (2009), 599.

6. S. Tashenov, A. Khaplanov, B. Cederwall, *Gamma-ray tracking and background suppression in the planned germanium array of DESPEC: A comparative analysis*, Nucl. Instr. and Meth. A604 (2009), 64.

Further papers with the author's contribution:

1. A. Persson, **A. Khaplanov**, B Cederwall and Ch. Bohm, *A prototype detector module for combined PET/CT or combined photon counting/standard CT based on SiPM technology*, submitted to IEEE Trans. Med. Imaging (2009).

2. M. Sandzelius, B. Hadinia, B. Cederwall, K. Andgren, E. Ganioğlu, I.G. Darby, M. Dimmock, S. Eeckhaudt, T. Grahn,P T.Greenlees, E. Ideguchi, P.M. Jones, D.T. Joss, R. Julin, S. Juutinen, **A. Khaplanov**, M. Leino, L. Nelson, M. Nyman, R.D. Page, J. Pakarinen, E.S. Paul, M. Petri, P. Rahkila, J. Sarén,

C. Scholey, J. Sorri, J. Uusitalo, R. Wadsworth, R. Wyss, *Identification of Excited States in the $N = Z + 2$ Nucleus ^{110}Xe: Evidence for Enhanced Collectivity Near the $N = Z = 50$ Double Shell Closure*, Phys. Rev. Lett. 99, 022501 (2007).

3. M. Sandzelius, E. Ganioğlu, B. Cederwall, B. Hadinia, K. Andgren, T. Bäck, T. Grahn, P.T. Greenlees, U. Jakobsson, A. Johnson, P.M. Jones, R. Julin, S. Juutinen, S. Ketelhut, **A. Khaplanov**, M. Leino, M. Nyman, P. Peura, P. Rahkila, J. Sarén, C. Scholey, J. Uusitalo, R. Wyss, *First observation of excited states in ^{172}Hg*, Phys. Rev. C 79, 064315 (2009).

4. M. Sandzelius, B. Cederwall, E. Ganioğlu, J. Thomson, K. Andgren, L. Bianco, T. Bäck, S. Eeckhaudt, M.B. Gomez Hornillos, T. Grahn, P.T. Greenlees, B. Hadinia, A. Johnson, P.M. Jones, D.T. Joss, R. Julin, S. Juutinen, S. Ketelhut, **A. Khaplanov**, M. Leino, M. Nyman, R.D. Page, P. Rahkila, J. Sarén, J. Simpson, J. Sorri, C. Scholey, J. Uusitalo, R. Wyss, *γ-ray spectroscopy of ^{163}Ta*, Phys. Rev. C 80, 054316 (2009).

5. K. Andgren E. Ganioğlu, B. Cederwall, R. Wyss, S. Bhattacharyya, J.R. Brown, G. de Angelis G. de France Zs. Dombrádi, J. Gál, B. Hadinia, A. Johnson, F. Johnston-Theasby, A. Jungclaus, **A. Khaplanov**, J. Kownacki, K. Lagergren, G. La Rana, J. Molnár, R. Moro, B.S. Nara Singh, J. Nyberg, M. Sandzelius, J.-N. Scheurer, G. Sletten, D. Sohler, J. Timár, M. Trotta, J.J. Valiente-Dobón, E. Vardaci, R. Wadsworth, and S. Williams, *Low-spin collective behavior in the transitional nuclei $^{86,88}Mo$*, Phys. Rev. C 76, 014307 (2007).

6. M. Petri, E.S. Paul, B. Cederwall, I.G. Darby, M.R. Dimmock, S. Eeckhaudt, E. Ganioglu, T. Grahn, P.T. Greenlees, B. Hadinia, P. Jones, D.T. Joss, R. Julin, S. Juutinen, S. Ketelhut, **A. Khaplanov**, M. Leino, L. Nelson, M. Nyman, R.D. Page, P. Rahkila, M. Sandzelius, J. Sarén, C. Scholey, J. Sorri, J. Uusitalo, and R. Wadsworth, *Nuclear levels in proton-unbound ^{109}I: Relative single-particle energies beyond the proton drip line*, Phys. Rev. C 76, 054301 (2007).

7. K. Andgren, B. Cederwall, J. Uusitalo, A.N. Andreyev, S.J. Freeman, P.T. Greenlees, B. Hadinia, U. Jakobsson, A. Johnson, P.M. Jones, D.T. Joss, S. Juutinen, R. Julin, S. Ketelhut, **A. Khaplanov**, M. Leino, M. Nyman, R.D. Page, P. Rahkila, M. Sandzelius, P. Sapple, J. Sarén, C. Scholey, J. Simpson, J. Sorri, J. Thomson, and R. Wyss, *Excited states in the neutron-deficient nuclei $^{197,199,201}Rn$*, Phys. Rev. C 77, 054303 (2008).

8. K. Andgren, U. Jakobsson, B. Cederwall, J. Uusitalo, T. Bäck, S. J. Freeman, P.T. Greenlees, B. Hadinia, A. Hugues, A. Johnson, P.M. Jones, D.T. Joss, S. Juutinen, R. Julin, S. Ketelhut, **A. Khaplanov**, M. Leino, M. Nyman, R. D. Page, P. Rahkila, M. Sandzelius, P. Sapple, J. Sarén, C. Scholey, J. Simpson,

J. Sorri, J. Thomson, and R. Wyss, *Gamma-ray spectroscopy of* ^{197}At, Phys. Rev. C 78, 044328 (2008).

9. B. Hadinia1, B. Cederwall, R. D. Page, M. Sandzelius, C. Scholey, K. Andgren, T. Bäck, E. Ganioğlu, M. B. Gómez Hornillos, T. Grahn, P. T. Greenlees, E. Ideguchi, U. Jakobsson, A. Johnson, P. M. Jones, R. Julin, J. Juutinen, S. Ketelhut, **A. Khaplanov**, M. Leino, M. Niikura, M. Nyman, I. Özgür, E. S. Paul, P. Peura, P. Rahkila, J. Sarén, J. Sorri, J. Uusitalo, and R. Wyss, *Identification of gamma rays from* ^{172}Au *and* α *decays of* ^{172}Au, ^{168}Ir *and* ^{164}Re, Phys. Rev. C 80, 064310 (2009).

10. A. Jungclaus, L. Cáceres, M. Górska, M. Pfützner, S. Pietri, E. Werner-Malento, H. Grawe, K. Langanke, G. Martínez-Pinedo, F. Nowacki, A. Poves, J. J. Cuenca-García, D. Rudolph, Z. Podolyak, P. H. Regan, P. Detistov, S. Lalkovski, V. Modamio, J. Walker, P. Bednarczyk, P. Doornenbal, H. Geissel, J. Gerl, J. Grebosz, I. Kojouharov, N. Kurz, W. Prokopowicz, H. Schaffner, H. J. Wollersheim, K. Andgren, J. Benlliure, G. Benzoni, A. M. Bruce, E. Casarejos, B. Cederwall, F. C. L. Crespi, B. Hadinia, M. Hellström, R. Hoischen, G. Ilie, J. Jolie, **A. Khaplanov**, M. Kmiecik, R. Kumar, A. Maj, S. Mandal, F. Montes, S. Myalski, G. S. Simpson, S. J. Steer, S. Tashenov, and O. Wieland, *Observation of Isomeric Decays in the r-Process Waiting-Point Nucleus* ^{130}Cd, Phys. Rev. Lett. 99 132501 (2007).

Chapter 1

Introduction

Germanium detectors have been a central tool in experimental nuclear structure physics studies which to a large extent are based on high-resolution γ-ray spectroscopy. The combination of excellent resolution with large sensitive volume and a high stopping power make high purity germanium (HPGe) detectors unique in their kind. The development of new more advanced detectors and methods of data analysis, however, continues to this day. It has been found that a two-dimensional segmentation of the detector surface enables a three-dimensional position sensitivity through the analysis of pulse shapes [1, 2]. Modern germanium detectors are therefore in many cases manufactured with segmented electrical contacts that are read out simultaneously through independent preamplifiers. The resulting sets of signals can be treated by pulse shape analysis (PSA) methods in order to obtain the positions of the individual interaction locations of a photon. γ-ray tracking can then be used to determine the path of the photon through the detector.

This feature is highly desirable in nuclear physics experiments as it can be used to greatly increase the efficiency of a spectrometer [3]. It also opens up the possibilities of new applications where previously only highly granulated detectors or detector systems with a large amount of collimator material were used. In particular, γ-ray imaging applications, including those with polarization sensitivity, are of great interest in today's medicine, astronomy and nuclear non-proliferation safeguards.

1.1 Photon interactions

A photon traversing matter has several interaction possibilities. Unlike charged particles, a photon suffers no continuous energy loss but looses energy at discrete interaction points. The cross sections of the possible interactions in germanium as a function of the γ-ray energy are presented in fig. 1.1. We see that Compton scattering and photoelectric absorption are the two dominating processes for the energies of 10 keV–10 MeV, common for nuclear de-excitations. Rayleigh scattering

also contributes in the lower energy range. For a typical γ-ray, a total absorption event will consist of a series of scatterings followed by a final photo-absorption.

The fact that all of the interaction points of a scattered γ ray may or may not be inside the sensitive volume of a detector presents difficulties in measuring its total energy. For incomplete energy collection, an event contributes to the so-called Compton distribution in a spectrum. At the same time, the kinematics of the interactions are not random, and with advanced analysis, this difficulty can be turned into an advantage.

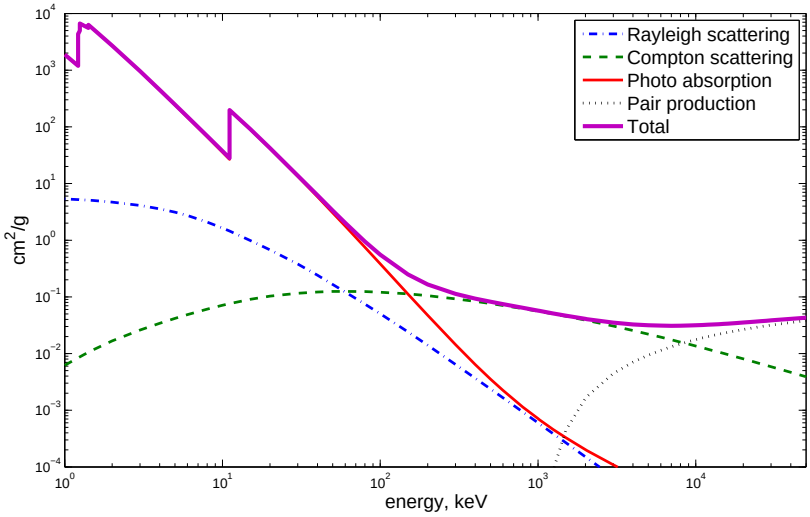

Figure 1.1: Photon cross section in Germanium [4]

For completeness, one should also mention that a photon can be absorbed in a nucleus resulting in a nuclear excitation. The de-exciting nucleus could emit a new photon or a particle. Such photo-nuclear reactions are highly dependent on the photon energies and the available states in a nucleus and are overall not common compared to the other modes of interaction.

1.1.1 Photoelectric absorption

A photon may transfer all of its energy to an atomic electron. This is known as photo absorption. Fig. 1.1 shows that the cross section for this process grows rapidly as the energy decreases. Since the electrons are initially bound, a part of the photon energy is spent to free the electron and the rest is transferred to the electron as kinetic energy. If E_{bind} is the electron binding energy and $\hbar\omega$ is the

energy of the photon, the kinetic energy of the electron is given by

$$E_{kin} = \hbar\omega - E_{bind}, \tag{1.1}$$

The characteristic edges in the photoelectric cross section are found at the binding energies of the atomic electrons in various shells, where, with increasing photon energy, a greater number of electrons becomes accessible.

A photoelectric interaction manifests itself as a point-like interaction in the context of large-volume solid-state detectors. Both components of the deposited energy - the fast electron and the x-ray photon (or an Auger electron) created when the vacancy left by the electron is filled - are typically stopped within 1 mm or less from the interaction point.

1.1.2 Scattering

Compton scattering is the dominant mode of interaction for photons in germanium for energies between 150 keV and 8 MeV, see fig. 1.1. In Compton scattering, the energy of an incoming photon is partitioned between a scattered photon and an atomic or a free electron. Due to the conservation of momentum, the momentum vectors of the initial photon, the final photon and the recoiling electron lie in a plane. The initial energy of the photon, E_γ, is shared between the scattered photon, E'_γ, and the electron, E_{e^-} according to

$$E'_\gamma = \frac{E_\gamma}{1 + \frac{E_\gamma}{m_e c^2}(1 - \cos\theta)} \tag{1.2}$$

$$E_{e^-} = \frac{\frac{E_\gamma^2}{m_e c^2}(1 - \cos\theta)}{1 + \frac{E_\gamma}{m_e c^2}(1 - \cos\theta)} \tag{1.3}$$

The energy transferred to the electron increases with the scattering angle, θ, and is greatest in the case of backscattering ($\theta = 180°$). It is also generally true that the typical energy transfer increases with the photon energy. It is common that a photon undergoes Compton scattering several times until its energy is reduced sufficiently for photo-absorption to become the more likely interaction. In the classical limit, $E_\gamma << m_e c^2$, scattering on free electrons, this reduces to Thomson scattering.

The scattering of a photon against an electron that remains bound after the scattering is known as Rayleigh scattering. Since the electron is not excited in the process, the atom as a whole absorbs the recoil momentum. Replacing m_e in 1.3 with an atomic mass leads to a energy deposit on the order of a few meV for typical x- and γ-rays and can be neglected in most applications. Since in Rayleigh scattering the incoming photon does not free the electron, its cross section decreases rapidly with energy and it is more likely to involve the most tightly bound electrons. The cross section also grows rapidly with the atomic number. In contrast, the less

tightly bound electrons tend to be the ones participating in Compton scattering (partially because they are more numerous).

1.1.3 Pair production

In a pair production event, a photon interacts with the electric field of a nucleus or an electron creating an electron and positron pair. The interaction with the larger nuclear field is far more likely. Unlike the other types of interactions, pair production has an energy threshold at twice the electron rest mass required by energy conservation. Any energy above 1022 keV is shared between the electron and the positron. Both particles are stopped in the vicinity of the interaction point. The stopped positron annihilates with an electron in the material, usually producing a pair of 511 keV photons. These generally need not interact close to the pair production point but will undergo a series of Compton scatterings and eventually a photo absorption in the same way as any other photons, and may also escape from the detector volume.

1.2 Photon detectors

Interactions of a γ-ray can be detected due to either the free charges they liberate (semiconductor or gaseous detectors) or photons generated (scintillation detectors) when energy is deposited in the detector material. In a semiconductor detector, electrons (and positrons) excited or created through one of the processes above create a cloud of secondary charges – holes (h^+) and electrons (e^-) – through ionization and multiple scattering processes. Such detectors have a superior energy resolution relative to scintillation detectors due to the small band gap energy which leads to a large number of excitations. In a semiconductor crystal with electrical contacts on the surfaces the liberated charges can be collected by an externally applied electric field. The charge pulses are integrated by a charge-sensitive preamplifier and can then be further processed by analogue or digital electronics.

Many types of semiconductor detectors exist. Silicon is commonly used for the detection of charged particles and low-energy photons. These detectors may be arrayed as thin wafers intended to track a particle as it traverses one wafer after the other. In applications where a particle's total energy is of interest, it is often implanted into a thicker silicon detector. Germanium is the material of choice for the detection of γ rays due to its greater atomic number and density. It also has a smaller band gap leading to better energy resolution. Both large-volume silicon and germanium photon detectors require cryogenic cooling in order to suppress the thermal noise. The thin silicon wafers used for charged particle detection may be operated at room temperature, although optimal performance is often achieved at temperatures below 0°C. Other semiconductor detectors include cadmium-zinc-telluride (CZT), that has a significantly higher efficiency than germanium but is not available as large single crystals, and diamond wafers that have outstanding timing characteristics, and can be used for example for beam detection.

In a scintillation detector, energy deposited in γ-ray interactions gives rise to photons (typically visible or in the near ultra-violet region). This light is in turn detected by a photomultiplier or a solid-state sensor such as an avalanche photo diode where an electronic signal is produced. A multitude of scintillation materials with varying properties exist. A plastic scintillator may be used for a fast detection of charged particles. Bismuth germanate (BGO) is the optimal scintillator if a high efficiency is the dominant requirement. Lutetium ortosilicate (LSO/LYSO) is the scintillator of choice in positron emission tomography (PET) where a good efficiency for 511 keV photons must be combined with a high timing resolution. Relatively good energy resolutions of NaI and CsI make these crystals suitable for γ-ray spectroscopy, while BaF_2 is well-known for its excellent timing resolution. A new scintillator – lanthanum bromide ($LaBr_3$) – possesses a good compromise of timing and energy resolution and a good efficiency, however, its use is at present limited by the high cost and the difficulty in the machining and handling of the crystals.

Photons of lower energies can also be detected using gaseous detectors. In this case interactions create e^--ion pairs that can be either collected onto contacts or induced to create an avalanche by a large applied electric field. In some cases scintillation can also be measured in a gas-filled detector and can even be combined with a measurement based on charge collection. Overall, gas-filled detectors are more common for detecting charged particles.

The energy resolution of a detector depends on several factors. The main contribution of the active detector material enters in the form of a statistical variation in the number of excitations created by the absorbed photon or particle. The number of excitations is the measurement of the energy and the standard deviation of this value contributes to the resolution and is combined with the other sources of noise. In addition to the observed charge pairs or photons, energy may also be deposited as molecular or atomic excitations or as phonons. Since for a given absorbed particle the total energy must be deposited in a combination of these forms, the variance in the number of detectable quanta is correlated with the variance in the number of the undetected ones. As a result, variance contributing to the energy resolution is decreased by the so-called Fano factor, whose value is 0.12 for germanium. Further noise sources are primarily electronic in nature and will depend on the circuitry used, temperature, purity of the materials as well as interference from other devices. Timing resolution is primarily defined by the speed with which charges or photons are created and collected. It also depends on the yield of excitations per unit energy of the incoming particle, since the signal-to-noise ratio will affect the influence of jitter on the timing of a pulse. An overview of various noise contributions can be found in ref. [5] where, in particular, a silicon detector is studied.

1.3 Pulse shape analysis and γ-ray tracking

The goal of pulse shape analysis (PSA) and γ-ray tracking is the reconstruction of the paths taken by scattered photons interacting with a detector on an event-by-event basis. A series of interactions of the types described above constitute a track of approximately point-like energy deposits. For γ-ray energies typical for nuclear physics ($\sim$10-10000 keV), the tracks will predominantly consist of several Compton scattering points and a final photo-absorption. Pair production becomes significant towards the high-energy end of the spectrum. In the events where pair production takes place, it is almost certainly the first interaction and the remaining ones constitute the tracks of the two annihilation photons. Rayleigh scattering is normally not detectable by these methods since the deposited energy in the scattering point is very low. While it can contribute to an uncertainty in the direction of the photons travelling through germanium, the scattering cross section is relatively low for most of this energy range and the scattering is predominantly forward-focused.

The task of determining the track of a γ ray is divided into two distinct problems. The first is to find the points within the detector where energy has been deposited. This is accomplished when granular or segmented detectors are used. This can result in very large numbers of readout channels – assuming that each detector element is readout independently, the number of channels grows quadratically with decreasing position resolution for a 2-dimensional detector. The PSA methods studied in this work allow a significant improvement in resolution for a relatively low granularity of a detector. The second problem is to determine the order in which the points found by PSA were visited, and in more complex cases with many interacting photons, to find which interactions belong to the track of a given photon and which do not. The main tool used by the tracking algorithms is the Compton scattering formula 1.3 due to its ability to relate the geometrical locations of interactions to the deposited energy. In many applications it proves to be useful to have information concerning the direction of the incoming photon or even just the position of its first interaction with the detector.

1.4 Applications

1.4.1 New generation of γ-ray spectrometers

Several germanium detector arrays are currently used in nuclear structure studies. The EUROBALL [6] array was operated until 2003 in Strasbourg, France. It consisted of three types of germanium detectors – ones with single tapered coaxial crystals, 4-crystal clover detectors and 7-crystal cluster detectors. Presently, these detectors are incorporated into the JUROGAM [7] array in Jyväskylä, Finland and the RISING [8] array at GSI, Germany. A more recent generation of arrays include EXOGAM [9], MINIBALL [10] and TIGRESS [11]. These newer detectors have all been manufactured with segmented outer contacts and thus increased granularity.

In the above-mentioned arrays large coaxial germanium crystals are used. Nevertheless, a significant part of the detected photons escape before a full absorption, resulting in spectra with a large contribution of Compton continuum. In order to counteract this effect and reduce the background, highly efficient BGO scintillation detectors surround the germanium crystals. These are used in anticoincidence with germanium, thus rejecting events where photons are incompletely absorbed in the Ge[1]. This technique greatly reduces the Compton background in the spectra. Unfortunately, it also rejects a large portion of the γ-rays. Furthermore, the Compton shields occupy much of the solid angle seen by the γ-rays emerging from a target chamber (on the order of 50%), further limiting efficiency.

The new arrays seek to overcome these limitations by using very closely-packed germanium detectors with tracking capability, eliminating the need for escape suppression. The schematic of the geometry of the new AGATA array is shown in fig. 1.2 – the 180 detectors needed to complete this array form a near-4π coverage. The photons that scatter in one detector and escape need no longer be rejected – they are likely to be absorbed in a neighbouring one. Pulse shape analysis finds individual interactions, and γ-ray tracking is not restricted to a single detector. The tracking algorithms are also intended to disentangle a large number of interactions that may occur simultaneously from high-multiplicity events in heavy-ion fusion reactions or as a result of a prompt γ-ray flash induced by bremsstrahlung from relativistic ions. Two new γ-ray spectrometers for nuclear structure studies, AGATA [12] in Europe and GRETA [13] in the USA, are currently being constructed. Each spectrometer employs PSA and tracking to overcome many limitations of spectrometers of the previous generations. The DESPEC array [14] is currently in the design stage and is aimed to also include imaging capabilities.

A further limitation of the conventional arrays is the Doppler broadening of the spectral lines that occurs in the experiments where the emitting nucleus has a large velocity during the decay. The Doppler-shifted energies can be corrected if the emission direction with respect to the velocity vector is known. In case of fast decays, the decay location can be assumed to be known (i.e. the target location). The emission angle of a photon is then given by the location of the first interaction point inside the germanium detector, and is limited by its opening angle relative to the point of emission. The advantage of a tracking array lies in its ability to locate interaction points, efficiently highly improving the granularity of the detector, resulting in a much finer Doppler correction. This capability has been tested using the AGATA prototype detector during an in-beam test [15] and later with the first asymmetric AGATA detectors at Laboratori Nazionali di Legnaro (LNL) [16].

The DESPEC array is proposed for the spectroscopy of the decaying recoils implanted at the focal plane of the Super-FRS at the future FAIR facility [14]. Similarly to AGATA, this detector array will take the advantage of tracking in

[1]The BGO shields are placed outside of the detector cryostats, i. e. in cases where a detector module is composed of multiple Ge crystals, the BGO shields detect the escape of photons from the module as a whole.

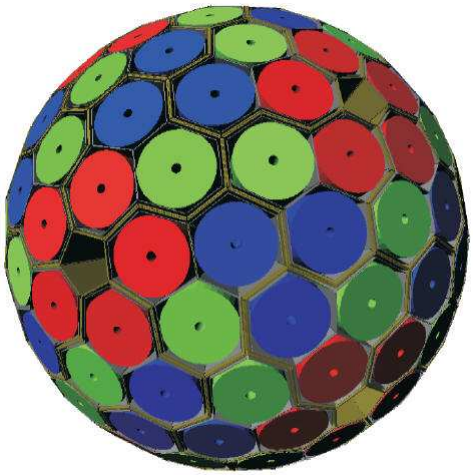

Figure 1.2: Schematic of the closely packed germanium crystals for AGATA.

order to increase efficiency, as well as to find the direction to the source of the radiation as in the case of γ-ray imaging, enabling the rejection of background that is not originating from the implantation detector.

1.4.2 γ-ray imaging

As has already been mentioned, a tracking algorithm is capable of estimating the direction to the source. In practice, since the Compton recoil electrons are normally not tracked, this direction will have a rotational degree of freedom, forming a cone of possible directions to the source. Nevertheless, such cones from many interactions can combine to an image. This is known as Compton imaging and has been applied primarily in γ-ray astronomy [17]. Conventionally, one relies on highly granulated detector systems. Segmented germanium detectors, however, may allow imaging using only two or even a single detector [18, 19].

In addition to γ-ray astronomy, γ-ray imaging is a highly important tool for non-invasive medical examinations. Both the gamma camera, as well as the positron emission tomograph (PET) may benefit from the advent of position-sensitive detectors [20]. In the recent years there has also emerged a significant interest for γ-ray imaging employed for national security and nuclear non-proliferation safeguards [18, 21].

Chapter 2

Germanium detectors

A germanium crystal of a diameter up to about 10 cm can be grown using present technology, allowing the manufacture of large detectors with high efficiency. Coaxial (more commonly, closed-end coaxial) detectors with an outer contact and an inner core and planar (rectangular or cylindrical) detectors with contacts on the flat sides can be made. All germanium detectors must be operated in a cryostat at a low temperature – typically that of liquid nitrogen – in order to suppress thermal noise. A comprehensive review of the development of germanium detectors starting with the early Ge(Li) detectors and describing the progress leading up to the upcoming tracking arrays can be found in ref. [22].

2.1 Manufacturing, impurity and surfaces

HPGe-grade germanium is obtained using the zone-refinement technique [23] where an ingot of germanium is subjected to successive melting and re-crystallization along its length. The impurities have a tendency to remain in the liquid phase rather than in the solid one and are thus, in effect, moved to the end of the ingot. The refined germanium is then melted. A seed crystal is dipped into the melt and withdrawn slowly, resulting in a growth of a large mono-crystal suitable for detector manufacturing. This crystal is later cut and machined to the desired geometry. During the growth process the impurity concentration in the melt is not constant, resulting in a varying concentration along the crystal that can range from a predominantly n-type at one end to p-type at the opposite end. For a detector cut from such a crystal, the impurity concentration is specified by the manufacturer at the top and bottom of the cut crystal. The exact variation is usually unknown, and a linear variation is assumed for most calculations. The typical impurity concentrations are $5 \times 10^9 - 2 \times 10^{10} atoms/cm^3$ and can be of either $p-$ (mainly B and Al) or $n-$ (mainly Li, O and P) type.

The contacts are typically made by adding a much higher impurity concentration to the crystal surface. Commonly boron implantation creates a thin ($\approx 0.3\mu m$)

$p+$ contact and lithium drifting creates a thicker (up to $0.7mm$) $n+$ contact. Detector contacts of both polarities have also been created by sputtering amorphous germanium (a-Ge) onto the crystal surface [24]. This technique is for the moment not wide-spread.

The contacts are manufactured in such a way that prevents injection of charges into the bulk of the crystal, thus greatly increasing the resistivity of the crystal. A significant leakage current may nevertheless be present on the uncontacted surface. An open surface, such as the side of a planar crystal between the two contacts, has a tendency to exhibit the properties of either $p+$ or $n+$ semiconductor and may not be depleted fully. These regions, known as surface channels, result in poor charge collection as well as trapped charge close to the surface that in turn changes the shape of the electric field at the edges of the detector [25, 26]. Passivation of the surface is required to counteract these effects. Several techniques exist [27], unfortunately, very little information concerning the exact technique used in the passivation of modern detectors is released, as it is proprietary to the manufacturers. The passivated surfaces can easily loose their properties if contaminated, resulting in high leakage current or loss of efficiency close to these surfaces. The vacuum of the detector's cryostat prevents contamination under normal operation. In some cases, however, outgassing the detector at an elevated temperature (≈70-80°C) is needed in order to remove contaminants. In some cases, in particular in planar detectors, a separate contact (guard ring) is placed along the edge of the detector so that any effect of excessive leakage current or the electric field deformations is reduced.

2.2 Depletion and biasing

As impurity atoms can easily contribute free charges, the detector volume needs to be depleted in order for the charge pairs (electrons and holes) created in γ-ray interactions to be measurable at the contacts. In an HPGe detector, depletion can be achieved by applying a high voltage of up to 5 kV between the contacts which are separated by up to around 3 cm. The high voltage also serves as the means of collecting the charges created by the radiation. The narrow depletion zone at the junction of the bulk germanium and the contact of the opposite impurity type is expanded when a reverse-bias high voltage is applied. As the voltage is increased, the depletion zone grows until finally reaching the other contact and the entire volume of the detector is depleted at the depletion voltage (V_d). The operation voltage (V_o) is then set at least 500 V higher in order to ensure a high charge mobility throughout the active volume. In a depleted detector, the impurity ions can be viewed as a fixed space charge distribution (ρ_s). The total electric field results from the combined effects of V_o and ρ_s. It is strong on one side of the detector where the two contributions have the same sign and weak on the other.

In a coaxial detector the field lines are concentrated at the inner contact due to the geometry. In order to counteract this effect the detector type and polarity are

chosen in a way that balances this effect (in other words so that the depletion starts from the outer contact). Using a $p-$type crystal this can be achieved by placing the lithium-drifted contact on the outside and the boron-implanted contact at the core. For a $n-$type detector, the contacts are reversed. Since the placement of a thick lithium contact on the outer surface creates a screen that absorbs low-energy photons, $p-$type coaxial detectors should preferentially be used where the detection of low-energy photons is unimportant or undesired.

A further advantage of $n-$type coaxial detectors is the higher tolerance to neutron damage common in γ-ray spectroscopy. Neutrons can penetrate to any depth into the detector, interacting elastically or inelastically with germanium nuclei. This causes displacement of the atoms from their positions in the lattice resulting in sites where holes can be captured, preventing their contribution to the signals. This effect has been observed to degrade the energy resolution of a detector [28] and can be removed only by annealing at $\sim$120-200°C. In an $n-$type detector, holes are travelling to the outer contact, while in a $p-$type detector holes drift to the inner contact. Since most of the germanium volume is closer to the outer contact, on average, holes will travel a shorter distance in an $n-$type detector, and consequently are less likely to to be trapped before reaching the contact. Thus, while both types of crystals receive an equal amount of damage, the performance degradation is normally lower in an $n-$type detector.

While the closed-end coaxial detector is the most efficient way to manufacture large detectors from the available crystals, planar detectors have proven useful in some applications, and, as will be shown in this work, a higher position sensitivity and tracking and imaging capabilities are possible with planar detectors. A raw crystal with a $\sim$10 cm diameter and a larger length is cut across in order to make a planar detector, resulting a crystal of at most 74×74 mm (with somewhat rounded corners). Since the detector contacts are symmetric and the arguments differentiating the n- and p-type coaxial detectors do not apply, planar detectors are usually manufactured from p-type germanium since higher level of purity is easier to achieve in this case. The thickness is normally limited to 20 mm or somewhat more, so that the crystal can be depleted at a voltage of at most 3000 V. Smaller planar detectors are used for high-resolution measurements at low energies. While it would be possible to make a significantly larger crystal by cutting along the raw crystal, this is generally not done because the impurity concentration varies along the length of the crystal. Such a planar detector would have a varying depletion voltage at different positions, resulting in irregularities in performance.

2.3 Charge mobility

The applied electric field causes the charges to drift towards the contacts (holes and electrons travel to the contact of opposite polarity). The dependence of drift velocities on the applied field and temperature has been studied by Mihailescu, *et al.* [29] for electrons and Bruyneel *et al.* [30] for holes and are plotted in fig. 2.1.

For low field strengths, the charge velocity increases linearly. Eventually, however, it reaches a state close to saturation. Germanium detectors are operated at a bias voltage well into the region where saturation begins.

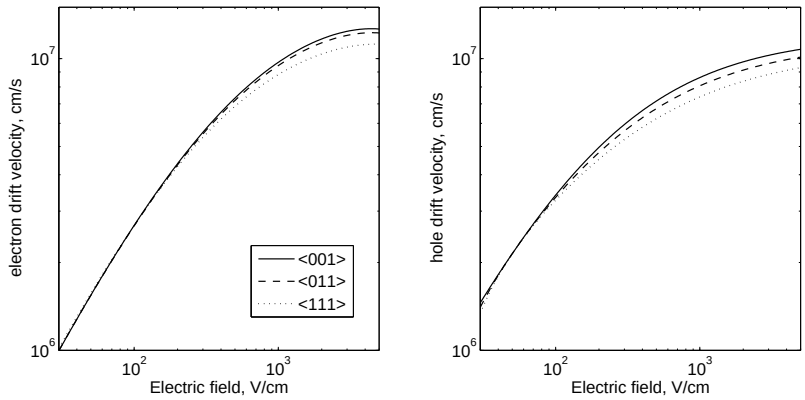

Figure 2.1: Drift velocities of electrons (left panel) and holes (right panel) as a function of the applied electric field in germanium at liquid nitrogen temperature.

Germanium, like silicon and carbon, forms a diamond crystal lattice pictured in fig. 2.2. The drift velocities are not identical for the three crystallographic directions and differ by as much as a factor of 1.3. Planar germanium detectors are normally cut so that the <001> direction is parallel to the applied electric field. In coaxial detectors, however, the motion of the charges can occur in any direction with respect to the crystallographic axes. The non-isotropic velocities will in this case result in a deviation between the direction of the electric field and the charge drift velocity vectors.

The presence of charges in the detector volume causes induced surface charges to appear on the electrical contacts. As the charges drift, the magnitude of the induced charges changes and finally reaches a maximum when the charges themselves reach the contacts[1]. The induced charges are collected on a capacitor in a charge-sensitive preamplifier and it is essentially this signal that is read out in a measurement.

2.4 Segmented detectors

Many modern state-of-the-art germanium detectors are manufactured with segmented contacts in order to obtain a high spatial sensitivity. Pulse shape analysis

[1]It is important to stress that the variation of the observed signals is caused by the charge drift and not by the collection of charges on a contact. This in in contrast to a scintillation detector, where the signal shape depends on the rate of emission and conversion of scintillation photons.

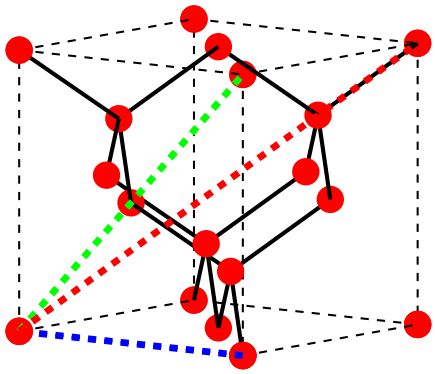

Figure 2.2: Examples of the <001> (blue), <011> (green) and <111> (red) directions in a diamond lattice. Note that due to the symmetry of the lattice, the properties of each crystallographic axis are repeated for a 90° rotation – for example, each edge of the cube belongs to the <001> set.

(PSA) has enabled a resolution of the positions of the interaction points that is about one order of magnitude more accurate than can be given by the dimensions of the physical segmentation [2, 31].

2.4.1 Planar detectors

A planar pixellated detector at KTH was used in the experimental parts of this work. The the dimensions of the germanium crystal are 58×58×21 mm. The cathode contact (boron implanted) has a 4-mm guard ring and a 5×5 pixel segmentation, with each pixel having the area of 1 cm^2. The anode contact (lithium drifted) is not segmented and covers the entire face of the crystal. A picture and a schematic of the detector crystal are shown in fig. 2.3 The signals are read out by charge-sensitive preamplifiers and digitized using a data acquisition system described in appendix A. Data from one of the double-sided strip detectors of the SmartPET imaging system [32] at University of Liverpool was also used for comparison with simulations in this work. The crystal dimensions are 74×74×20 mm. Both contacts are segmented into 12 orthogonal strips with a 5 mm pitch, surrounded by a 7 mm guard ring. Details concerning the readout and data acquisition for this detector can be found in ref. [32].

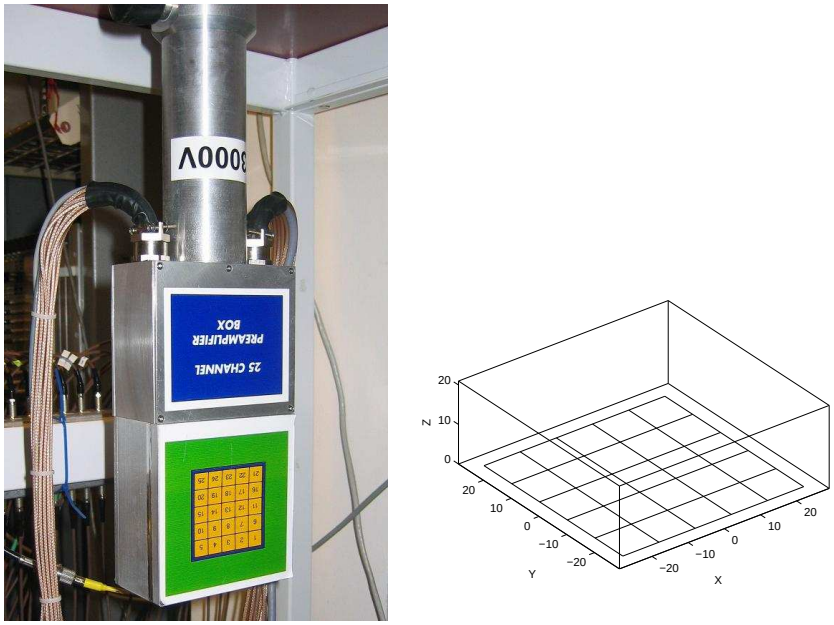

Figure 2.3: The KTH 25-pixel detector (left) and a schematic of its segmented crystal (right).

2.4.2 Coaxial detectors

The majority of germanium detectors are manufactured in the so-called closed-end coaxial geometry. Making a cylindrical detector crystal uses the grown raw crystal in the most efficient way. Such a crystal results in a thickness too large to be depleted with a reasonable voltage (without Li compensation). One of the contacts is therefore placed in a central bore hole, resulting in an inter-contact distance of ∼4 cm at most. The bore hole almost never extends all the way through the cylinder, but ends 1-2 cm from the front surface. In this way more germanium is retained, and, more importantly, a non-contacted surface is avoided on that end of the crystal that would otherwise result in a dead layer of germanium. So-called clover coaxial detectors are studied in particular in this work.

Detectors consisting of four coaxial crystals have been constructed for a number of arrays starting with EUROBALL. The four crystals are cut on the sides in order to minimize the empty gaps both between the crystals and on the outer side of the module. The resulting shape is reminiscent of a four-leaf clover, giving the detector its name. The crystals are also usually tapered on the front to facilitate packing in a spherical configuration around a target chamber. Some of the clover detectors have been manufactured with a longitudinal segmentation, where each crystal is given

four segments, as for example in the EXOGAM array. This increases the granularity of the detector to 16 segments as seen from the front of the module, resulting in an improved Doppler correction and polarization sensitivity. A full 3-dimensional sensitivity, however, cannot be achieved since longitudinal segmentation provides no sensitivity along the depth of the crystal. A 2-fold depth segmentation has been additionally implemented in the clover detectors of the TIGRESS array. This segmentation line is placed at 30 mm from the front of the detector. In this work, the idea of higher-fold segmentation of clover detectors has been investigated. In particular as a candidate for the DESPEC array, 12- and 16-fold segmented crystals were considered. The EXOGAM and TIGRESS detectors are based on crystals of a 60 mm radius and 90 mm length. A detector from the EXOGAM array is shown in fig. 2.4.

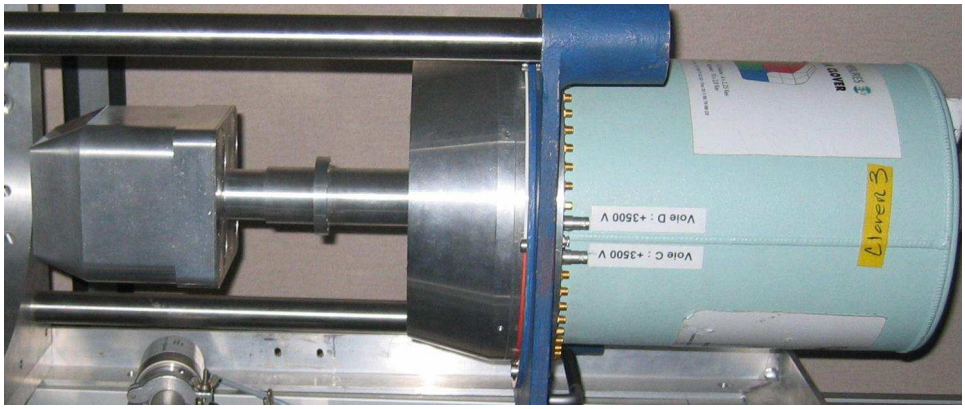

Figure 2.4: EXOGAM clover germanium detector.

2.5 Signal formation

When referring to pulse shapes in segmented detectors the concepts of current pulses and charge pulses are often used. The current pulses are the raw signals from detector contacts. These are normally not read out directly in a germanium detector (or in other types of detectors where no internal amplification occurs). A charge-sensitive preamplifier integrates the current pulses and the resulting charge pulses are further analysed. This section gives examples of charge and current pulses and their dependence on interaction position. Pulses shown here have been calculated using the method presented in section 2.6. This technique can be used to calculate signals resulting from arbitrary interaction location.

2.5.1 Current and charge signals

As both the motion of electrons and holes contribute to the formation of electrical signals, the shapes of the pulses consist of two components. Consider a contact at a positive potential. Electrons are attracted to this contact while the holes are repelled. At the moment of the creation of the charge cloud, both charges are in the same location and no charge is induced. As the electrons drift towards the contact their contribution to the signal grows while the contribution of the holes diminishes. A similar situation is seen on the opposite contact, with the polarity reversed. In case of a segment that collects the charge, both hole and electron components have the same polarity resulting in a **net** signal. In segments close to the one collecting a net charge, the contributions of the two charge species to the current signals are typically of opposite polarities and are in some cases bipolar. These signals result in a zero net charge signal, however, a positive, negative or bipolar **transient** pulse is created. An example of a current pulse in the KTH pixel detector is shown in fig. 2.5 and the corresponding charge signal is shown in fig. 2.6. In this case the interaction is located in the central segment 13 and results in a bipolar charge signal in the neighbouring segment 14. Note that an unsegmented contact always receives a net signal. The full response to a single interaction is therefore a pair of net signals (from the unsegmented contact and one of the segments) and transient pulses from the remaining segments.

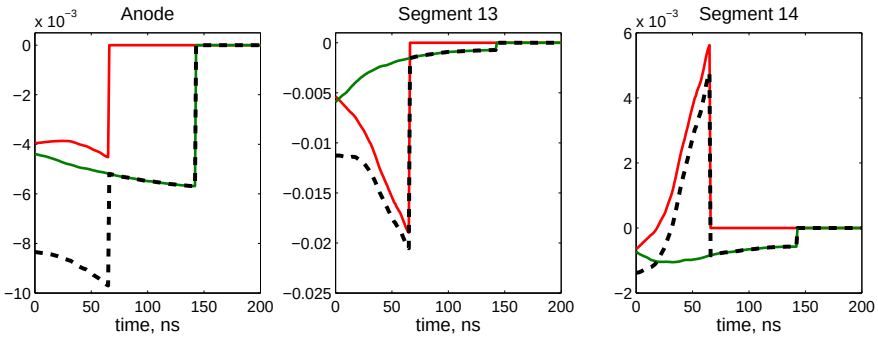

Figure 2.5: Current pulses from the anode and segments 13 and 14 for an interaction in segment 13. The contribution of holes is shown in red, electrons in green and the total in black.

2.5.2 Pulse shape vs. interaction position

Characteristic pulse shapes are observed for interaction points at different positions with respect to the contacts. Say the interaction is close to the the sensing contact and that it is the positive contact of the detector (usually the lithium-drifted

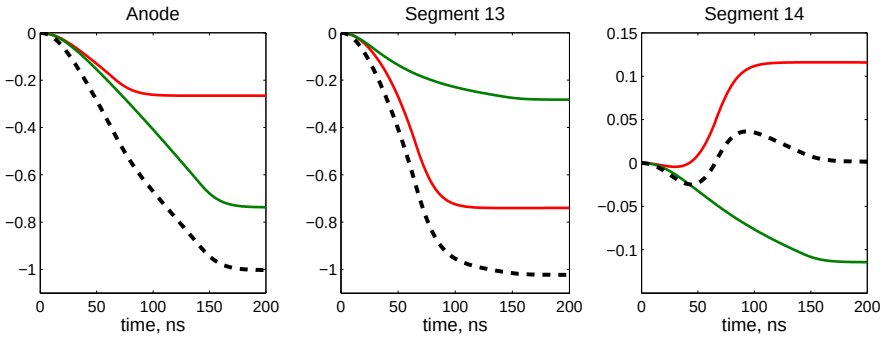

Figure 2.6: Charge pulses read out from the preamplifiers of the anode and segments 13 and 14 corresponding to the current pulses in fig. 2.5. The contribution of holes is shown in red, electrons in green and the total in black. The charge pulses are smoothed due to the finite bandwidth of the preamplifier.

contact). Electrons are then quickly collected contributing to a small part of the signal's amplitude. Holes on the other hand recede from the contact. The hole contribution is strong in the beginning while they travel through the volume where the contact's sensitivity is greatest, but contribute less and less as they approach the opposite contact. In other words this creates a signal whose leading edge rises quickly in the beginning and slowly thereafter. The same interaction results in an entirely different signal if measured on the negative contact (usually, boron-implanted contact) – the quick collection of the electrons on the far-away contact is largely unnoticed, while the holes' contribution increases gradually until its maximum close to this contact. This results in a signal that rises slowly in the beginning and fast later on. A measurement of the pulse shape, therefore, provides information about the depth of the interaction, in fact, a very simple timing algorithm can produce good results [19, 31]. The positions in the other two coordinates can be obtained by electrically segmenting the contacts. In this case, analysis requires the consideration of the simultaneous signals from segments neighbouring to the one that actually collects the net charge.

While it is possible to segment the contacts in two dimensions producing a sufficient granularity to match the position resolution in the depth coordinate, it is not necessary – a rather small number of contacts (and thus, readout channels) in combination with PSA can provide an equally good position resolution. The induced charge is distributed over the contacts - the higher charge density is of course found in the area closest to the interaction point, yet the entire surface will sense some signal. If the contact is broken up into electrically insulated segments, the induced charge is similarly divided. Unless the charge cloud is exactly at the border of two segments, only one collects the net charge. The neighbouring contacts

sense a smaller amount of induced charge and this charge will be present only during the drift time. Once collected at one of the segments, the charge can no longer induce signals in the other segments. This type of signals is known as **mirror** or **transient signals**.

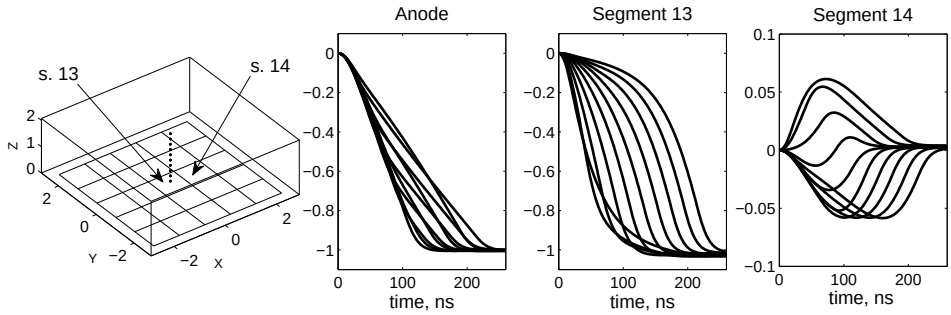

Figure 2.7: Charge signals from interactions at varying depths in segment 13. Interaction positions are shown on the left. The pulses with fast rise times of segment net pulses (segment 13) and positive transient pulses (segment 14) correspond to positions close to the segmented surface. Transient pulses of lower amplitudes are observed in corver-to-corner neighbours of the net charge segment and lower still in more distant segments.

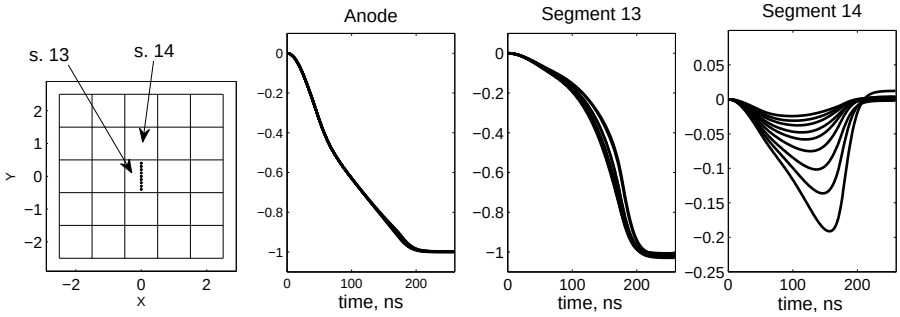

Figure 2.8: Charge signals from interactions at varying lateral positions in segment 13 at the fixed depth of 15 mm. Interaction positions are shown on the left. The pulses with large transient amplitudes in segment 14 correspond to interactions closer to segment 14.

Figures 2.7 and 2.8 show examples of possible shapes of charge signals in the KTH planar detector when the interaction depth or lateral position, respectively,

are varied. In general, the closer a segment is to the interaction point the more prominent is its transient signal. Furthermore, rise time, time to maximum and the polarity of the transient signals change with the depth of the interaction. A similar, although a less intuitive effect can be seen in a coaxial geometry where the outer contact is segmented. All of this information combined can be used to obtain the three-dimensional position of the interaction points of a γ-ray.

2.6 Simulation of pulse shapes

The pulse shapes arising from interactions of photons at arbitrary positions in the detector volume can be calculated. While for a few simple geometries it is possible to calculate an approximation analytically [1], in general, numerical methods must be used. A dedicated software was written for this task. The following outlines the procedure used to calculate pulse shapes.

2.6.1 Electric field

A basis for pulse shape simulations is the knowledge of the electric field within the detector. This problem is generally solved numerically as a steady state of the detector when the operation voltage has been applied and the final depletion of the crystal has been reached. The electric field is then a combination of the effects of the potential applied at the contacts, the space charge distribution left behind when the free charges have been removed from the impurity atoms, as well as effects of any surface charges that can arise if a surface acquires an impurity concentration.

The finite element method package COMSOL Multiphysics (previously known as FEMLAB) [33] has been used in this work to determine the electric field. With the geometry defined, this program generates a 3-dimensional grid and the field is calculated in the vertices. This grid is based on tetrahedrons whose size is set adaptively depending on the proximity to detailed parts of the model. A number of user-controlled parameters define the resolution of the grid either globally or for selected surfaces or volumes of the geometry. This is very useful since in segmented detectors the field is complex in the very narrow gaps between the contacts while relatively uniform throughout most of the detector volume. Adaptive grid scaling allows to define the field in the gaps with a high resolution while maintaining a manageable total number of grid vertices. Grids with up to approximately 500000 points have been used in this work.

The software solves the Poisson's equation 2.1 with the given boundary values and charge distributions.

$$\nabla^2 \varphi = \frac{\rho}{\epsilon} \tag{2.1}$$

For electric contacts, a fixed potentials are used as the the boundary values – either ground or the applied high voltage. For non-contacted, passivated surfaces the

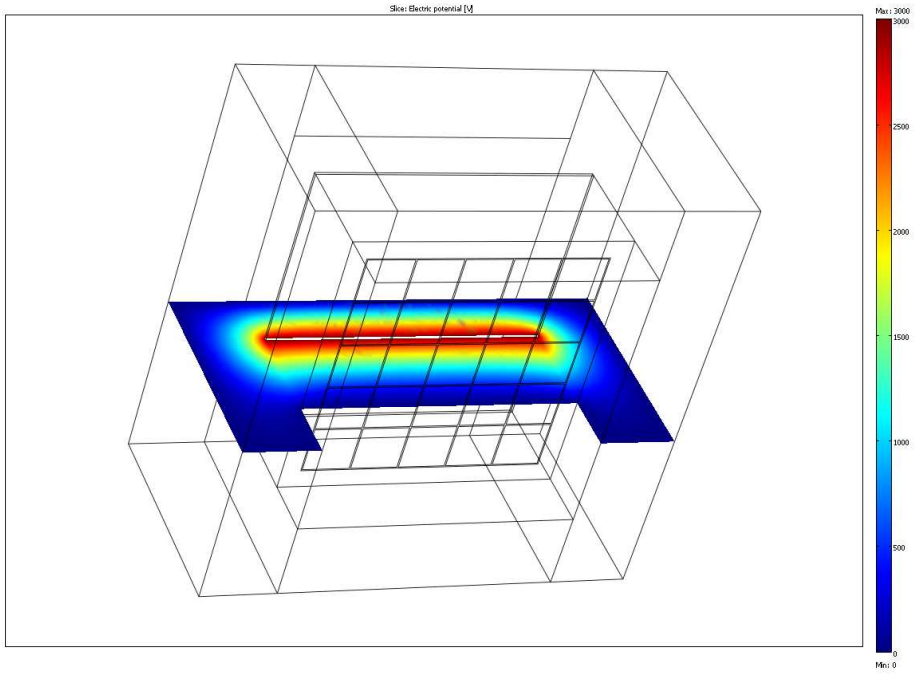

Figure 2.9: The potential map is shown for a slice through the KTH pixel detector. Here, a positive surface charge is included on the edges of the detector.

situation is more complicated[2]. A convenient way to treat these is by defining an outer enclosure which is grounded. This is the case with most germanium detectors, although in some cases insulator material may also be present. The passivated surfaces are then defined by a continuity condition or alternatively as a surface charge. As an example of such a calculation, the model of the KTH planar pixel detector implemented in COMSOL Multiphysics is shown in figure 2.9. A grounded outer enclosure is used here except around the pixellated side. This was done in order to prevent the software from generating a fine grid on the outside of the detector close to the gaps between the pixel contacts, that would lead to large increase in calculation time. Instead, a symmetry condition is used here. Since both the pixellated contact and the enclosure are set to ground potential, this approximation has a negligible effect, as opposed to the HV contact, which is surrounded by grounded surfaces.

[2]The passivated edge tends to be the most uncertain part of an electrical field simulation. While the contacted surfaces can be considered to be conductors at a well-defined potential, the exact properties of the passivated surfaces are rarely known and may not be constant over a detector's lifetime.

If the detailed simulation of the effects close to the edges of the detector is neglectable, the detector can be simulated without the enclosure, using symmetry conditions at the passivated surfaces. This provides acceptable results for planar detectors with wide guard rings or for coaxial detectors where only few interactions occur close to the passivated surface at the back of the crystal.

The electric field generated in this way was then exported and stored in files. Using this data, the pulse shape calculation was done in Matlab [44]. While convenient for the reasons described above, the irregular grid is quite difficult to use since it requires interpolation in order to find a value of the electrical field in an arbitrary point. In order to speed up this process, the grid data was sorted into blocks corresponding to small volumes that were then used for interpolation. Nevertheless, the E-field interpolation constituted the most processor-intensive part of pulse shape generation routine used in this work.

2.6.2 The weighting field method

In order to calculate pulse shapes, we need to determine the current flowing in or out of a detector contact as a function of time due to the movement of the charge cloud created in a photon interaction (let us call this the *test charge*). This is equivalent to determining the variation of the charge induced at the contact as a function of time. The induced charge is related to the electric field created by the test charge entering the contact. A determination of this quantity generally requires an integration of the electric field on a surface close to the contact and constitutes a rather challenging problem for arbitrary contact configurations and test charge positions. The solution to a relatively simpler reciprocal problem, however, provides the same result according to the Shockley-Ramo theorem [34, 35]. The electrostatic coupling between the test charge and the sensing electrode is described by the weighting potential (and the corresponding weighting field) which is given at the contact and is calculated at the location of the test charge. The induced current at the contact is then given by

$$I = q\overline{v} \cdot \overline{E}_w, \tag{2.2}$$

where $\overline{v}$ is the velocity of the charge and $\overline{E}_w$ is the weighting field at its current location. $\overline{E}_w$ only needs to be calculated once for each segment and can be reused for arbitrary locations of the test charge. Note that a weighting field is a construct used in calculation and not a physical field.

In a general definition proposed by Hamel and Julien [36, 37], the weighting field for a contact is given by a difference between the real field in the detector and a field obtained when the potential of that contact is incremented by some value (most conveniently 1). This procedure results in a weighting field where the effects of all constant space charges and all operating voltages vanish, leaving the additional field due to the increment as well as the effect of the increment on the material (i.e. the material polarization).

In practice, the weighting field for a contact is calculated using the full geometry of the detector where the potential at the contact in question is set to unity and at all remaining contacts to zero. The space-charge distribution is also set to zero, however, the material properties are left in place[3]. Here, weighting fields were calculated using a procedure identical to the calculation of the real field with the exception of the modified boundary conditions.

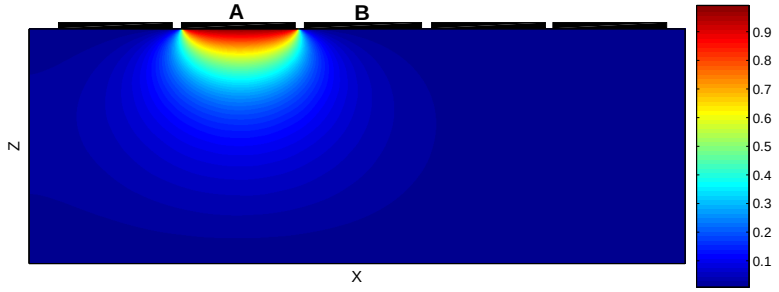

Figure 2.10: The weighting potential for segment A calculated using FEMLAB.

An example of a weighting potential associated with a weighting field[4] for one of the contacts (segment A) of a planar detector is shown in fig. 2.10. A charge moving along the z-axis towards the segment A experiences a continuously growing weighting potential all the way to the contact - this is a charge signal. A charge moving towards the neighbouring segment B encounters a potential that first increases and then reduces to zero (the contact itself is set to ground) - this is a transient charge.

2.6.3 Preamplifier response

The raw current pulses are in practice never treated directly, rather they are passed through a charge-sensitive preamplifier situated directly within the detector cryostat structure. In many cases the FETs of the first stage of preamplifiers are in the cold part of the cryostat in order to minimize thermal noise. A charge-sensitive preamplifier integrates the current pulse resulting in a signal proportional to the total collected charge. Ideally, the impulse response of such an integrating preamplifier is a step function. Realistically, its rise time is on the order of a couple of tens

[3]The condition for the validity of this simplification is linearity of the problem. This could be violated if, for example, the field of the test charge changes the space charge distribution.

[4]For segmented detectors, images of weighting *potentials* tend to be easier on the eye since the field is very large inside the segment gap, making a colour scale nearly uniform elsewhere. Furthermore, the vector components are easily visualised as the gradient of the scalar potential field.

of ns and it decays back to zero exponentially with a typical time constant of 50 μs. This decay time is essential from the point of view of the maximum signal rate for a detector since a preamplifier signal needs to stay in its operation range even if some pulses may be superimposed. The measurable charge signals are calculated by folding the calculated current signals with the preamplifier response function. This is illustrated in fig. 2.11. Note that a transient current pulse is bipolar and results in a 0 net charge signal for times greater than the charge collection time, in contrast to the net charge signal which reaches a value proportional to the collected charge.

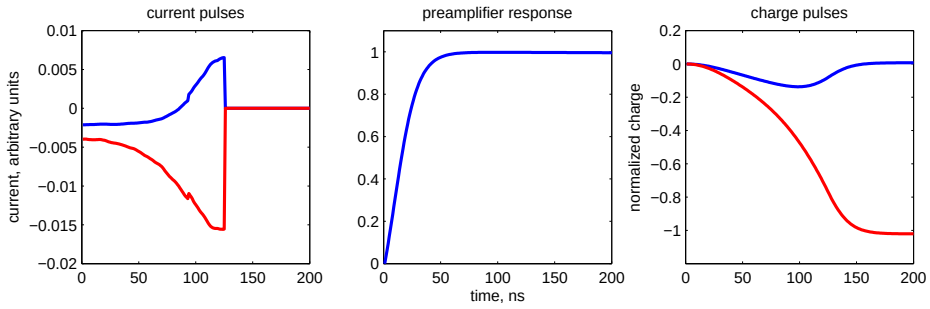

Figure 2.11: **Left:** calculated current pulses for a transient (blue) and net (red) charge signals. **Middle:** preamplifier impulse response function. **Right:** charge pulses as measured at the output from the preamplifier. The discontinuity in the current signal at ∼90 ns is due to the collection of one of the charge species.

2.7 Detector characterization

Most PSA algorithms rely on a set of accurate pulse shapes to be available for some interaction locations (basis signals). These can be calculated as described above or measured using a detector scanning set-up. Scanning a detector is a lengthy procedure and for multi-detector systems such as AGATA it is unrealistic to scan all detectors. Instead, calculated signals can be used once they have been verified using scanning data.

In the conventional scanning technique [1, 38], a collimated source, usually ^{137}Cs emitting 662 keV photons, is used to irradiate the detector. Two types of measurements can be performed – singles and coincidence scans. In either case, a collimated source is usually attached to a x-y positioning table controlled by a computer. The stationary detector is then scanned over a grid of positions. In a singles scan, subsequent off-line analysis can select single-segment and/or full absorption events. The advantage of a singles scan is that it can be performed rather quickly since interactions at all depths of the detector are measured simultaneously. The analysis of

this type of data makes it possible to verify the crystal orientation as well as to find and localize defects that may not be evident in, for example, an energy resolution measurement.

A coincidence scan is required to measure interactions at specific locations within a detector crystal. In order to determine the third co-ordinate of an interaction, photons that Compton scatter in the scanned detector at a specific depth at $\sim 90^\circ$ to the direction of the injection beam are detected. These are selected by slit collimators and detected in scintillation detectors, commonly BGO. A 662 keV photon scattering at 90° deposits 374 keV in the detector being scanned and 288 keV in a coincidence detector. Coincident events, where both detectors are hit, are acquired. Energy gates can then be set in order to minimize the contribution from events with more than a single scattering.

A number of alternative ideas for scanning have been proposed. In one such, the collimated source is replaced with an uncollimated source emitting positrons [39]. The resulting 511 keV annihilation photons are used for scanning – one is detected in a position-sensitive detector, thus determining the direction of the other, which is scattered in the scanned detector and stopped in a coincidence detector. The advantage of such an approach is that the entire detector is irradiated at once. However, in practice, good efficiency is nevertheless difficult to reach primarily due to the low efficiencies of the currently available position-sensitive detectors with sufficient spatial resolution. Another approach is to use singles data when the detector is irradiated with a collimated source from a number of directions [40]. The pulse shapes are then correlated, selecting interactions at the intersections of collimator beams. This is, at the very least, quite challenging, since very similar pulse shapes may originate from different interaction points or combinations of multiple interactions.

Due to the sizes of the collimators, the interactions in a scanning measurement are localized to within a few mm in each co-ordinate. This can result in pulse shapes with significant variation, especially if the scanning spot is close to a segmentation boundary. While averaging pulses removes noise, it is often not reliable since the more unusual pulse shapes will not be represented. Therefore, when scanning data was analysed in this work, no averaging was used, rather the reconstruction was performed on an event-by-event basis.

Chapter 3

Pulse shape analysis

3.1 PSA methods

A variety of PSA methods have been implemented. A great source of motivation in this area are the AGATA and GRETA projects where PSA is an integral part of the on-line data analysis. While it is beyond the scope of this thesis to detail all of these methods, it is interesting to compare some of the ideas that are being considered.

It is possible to generate pulse shapes for the interactions on a grid, chosen so that the resulting pulses form a complete (or rather a sufficient) basis. Interactions at arbitrary locations are then represented using either the closest basis point or an interpolation between a set of basis points. The challenge is to find the correspondence between a measured pulse and a typically very large set of pre-computed basis pulses. Grid search and particle swarm optimization are two examples of algorithms where a sub-set of the basis pulses is compared to the measured signal using a χ^2 criterion, resulting in a better-fitting sub-set until the search converges to a single (or several) point(s) [15]. The matrix method, more thoroughly detailed below, considers linear combinations of possible basis points. It is also possible to perform a wavelet transformation of both basis and experimental signals and then fit the wavelet coefficients. An artificial intelligence technique, called genetic algorithm, has also been applied to pulse shape analysis [41]. This method treats the interaction points as an evolving population, where individuals' survival depends on their fitness, i.e. similarity to the measured signal. The matrix method, originally described in ref. [42] and employed and presented in detail in this work, also falls into this general category.

Another approach relies on parametrising a characteristic set of features, common to all pulses, such as rise times, polarities, magnitudes and times to maximum of mirror signals. These parameters are then defined as a function of the detector position, and a given pulse can be quickly assigned to a position. The drawback of this approach is that superpositions of signals from nearby interactions result

in new values of such parameters. Thus it is most likely to be useful in detectors where multiple interactions in a segment or in adjacent segments are unlikely, as is the case with double sided strip detectors (DSSD) [19]. The main advantage is the speed of such analysis. These characteristics make the parametrization approach useful in medical imaging applications, where a system must be able to cope with large rates of single events.

3.2 Timing

In any pulse shape analysis method that performs a comparison of a measured pulse shape to a basis, it is extremely important that the two are aligned in time. A poor time alignment results in incorrect fitting, as can be seen in fig. 3.1. The greatest discrepancy between the two unaligned signals is in the leading edge of the pulse, thus a least square or similar algorithm would find a basis pulse that minimizes this discrepancy, while largely disregarding all other features in the waveform, such as the amplitude or polarity of the image charges. In the example in fig. 3.1, the experimental signal is delayed with relation to the basis signals. One can see that the algorithm picked a basis pulse with the lowest possible rise time to compensate.

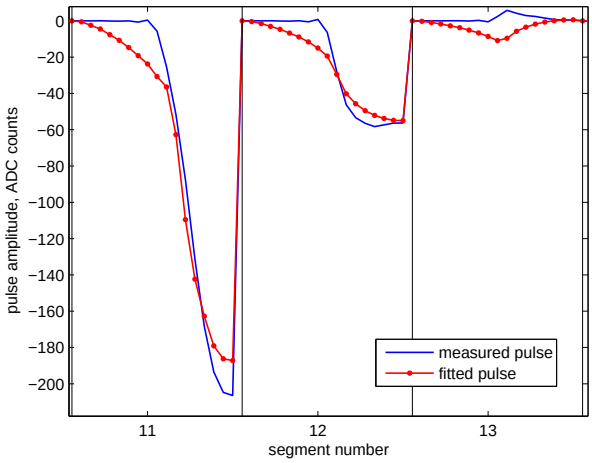

Figure 3.1: Pulse shape fit with erroneous timing. Here, the measured pulses are delayed in comparison to the basis pulses.

The standard technique for timing in gamma spectroscopy is constant fraction discrimination, CFD. This method yields best results for detector pulses of a constant shape and arbitrary amplitude. Since pulse shapes in a germanium detector are far from identical, a shaping filter must me applied prior to CFD (using for

example a timing filter amplifier, TFA). The digitization of pulses offers an alternative. Pulses can be fitted to known pulse shapes with known timing references, while treating the time-zero of the measured pulse as a free parameter. For pulses with a well-understood behaviour, an analytical function can be fitted to the pulse to determine timing. This is the case for the planar detector geometry, where full-energy pulses are essentially linear.

Consider a planar detector with unsegmented contacts where the dimension of the contacts is much greater than their separation. The relevant weighting field is then essentially uniform and thus the induced current on either contact is constant until the charge is collected[1]. This results in a linearly increasing charge signal. Considering that there are two charges in motion, the signal consists of a sum of two straight lines. Since the two contributions have generally a different duration the resulting total is a line consisting of two segments. A good timing can thus be obtained by fitting a straight line to the first segment of such a pulse and finding its intersect with the baseline. The segmentation of one of the contacts does not change the situation significantly other than to split the signal between the segments. Thus the total signal from all segments of a planar detector can be used for timing, this is illustrated in fig. 3.2. In the case of a pixellated detector this timing signal can be also simply be taken from the full-energy contact.

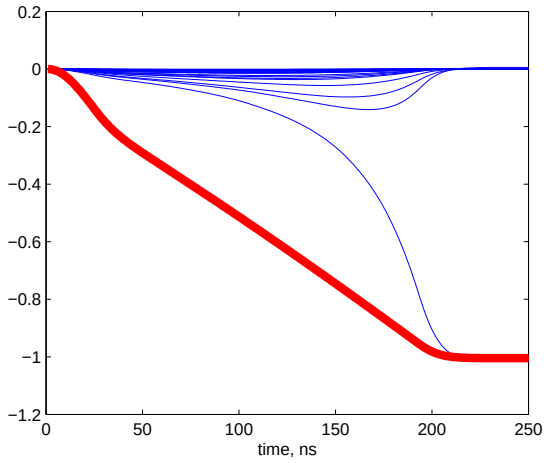

Figure 3.2: Summation of signals. Total signal is shown as a thick line.

This method has been used in most of the analysis of the simulated data and in some cases for the experimental data. The summation of the pixel/strip pulses

[1]Provided that the drift velocities are close to saturation, which is a reasonable approximation in a normally biased detector.

must be considered from the point-of-view of noise. For uncorrelated white noise, the resulting total pulse will be have a much lower noise level due to averaging, this makes the method very promising in the ideal situation of a simulation. In practice, electronic pick-up is often a large component of noise. In this case, the noise may be correlated in all channels and the summation results in the amplification of the pick-up by a factor equal to the number of segments summed. Thus when any algorithm dependent on pulse summation is implemented, there is a danger that the system will treat pulses incorrectly, or otherwise behave unpredictably when operated with a source of a pick-up noise.

A robust timing method is based on a fit to a measured pulse using a basis of calculated pulses that are either allowed to be shifted in time or are stored for a number of time shifts. This can be done using either summed pulses from a segmented contact or pulses from a full-energy contact. Figure 3.3 shows calculated and measured pulses from the anode of the KTH planar detector for interactions at different depths. Since, in the case of a planar detector, the net charge pulses vary only slightly with the lateral position, it is sufficient to consider a set containing only pulses from different depths. For a coaxial detector, this set should be expanded to a greater number of positions in order to fully represent the response. For completeness, it can be noted that the entire pulse shape basis (including net and transient signals) used for position determination can be stored with a range of time shifts. This option, however, while mathematically the most complete, would complicate the fitting procedure to a truly unmanageable degree.

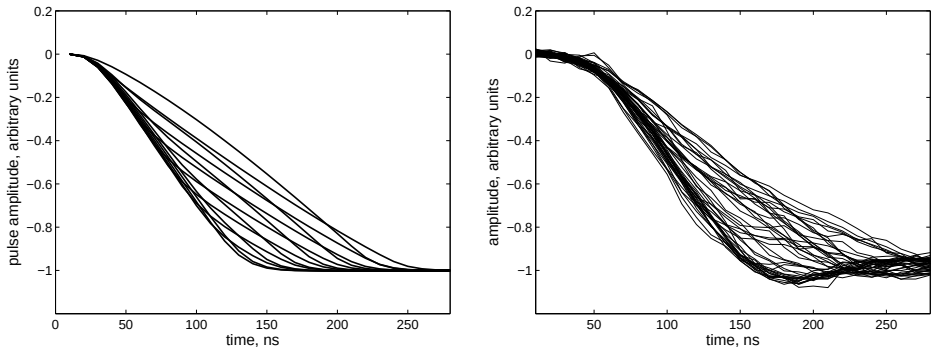

Figure 3.3: Calculated full-energy pulses from 14 depth positions for the KTH planar detector (left panel). Measured full-energy (anode) pulses (right panel). Approximately 40 measured pulses are shown. Note that here the pulses do not start at time zero, but at common reference time, shifted by +20ns.

At the end of this work, the timing algorithm included both ideas: a fast straight-line fit to the full-energy pulse followed by a fit to a set of pulses shifted

by 1-ns steps up to about ±10 ns (one ADC sample). In order to accommodate shifts smaller than the ADC sample period, the timing pulse had to be re-sampled at 10-fold increased rate. Once the best match is found, the signals are decimated to the original sample rate, but with a new time shift.

3.3 The matrix method

The task of deducing the position information from the pulse shapes becomes particularly complex when more than one segment in a crystal is hit. Provided that there are not at least 2 segments separating the target segments, one must take into account the superposition of transient signals from different interactions (in case of one-segment separation) and possibly of image signals with charge signals (in case of hits in adjacent segments). Such events are far from uncommon and cannot be discarded while maintaining a good efficiency of the detector. In order to deal with such situations other than by omission of channels containing superimposed signals, the measured signals must either be matched to a set of signals containing all possible superpositions or the PSA algorithm must be able to return more than one signal for a given event. The latter is the case for the matrix method [42].

Consider a number of point-like energy deposits and a set of measured pulse shapes. Both may be seen as vectors. The former, $\overline{x}$, is a list of energies deposited in all locations, where a few positive entries represent the interaction points and their energies. The latter is a digitized signal waveform, $\overline{s}$. The system that relates $\overline{x}$ to $\overline{s}$ is then a matrix in which one dimension matches the number of the locations considered and the other, the length of the digitized waveform. In short, such a system could be written as

$$M\overline{x} = \overline{s} \tag{3.1}$$

A matrix, M, that fulfils the requirement of this system is one where the columns are the waveforms arising from interactions in a set of points in the detector. This is a linear equation system; in other words, it is a necessary assumption that the signal from two interactions is the sum of the signals from each constituent interaction on its own.

While equation 3.1 appears extremely simple, the matrix M contains a vast amount of information. It is, however, possible to reduce the amount of data greatly, while preserving enough information for a reasonable solution. A further complication is that the solution $\overline{x}$ to eq. 3.1 may well include negative values – these are, however, unacceptable considering that the values are the deposited energies. Thus the system must be solved with a non-negativity condition. A further condition should be that the number of non-zero elements in $\overline{x}$ is small – after all it is highly unlikely that hundreds of points in a detector are struck simultaneously. The following section explores the matrix method in detail.

The matrix method was of particular interest for the analysis in this work due to its flexibility with respect to the input data. It naturally includes the facility to assign multiple interactions to an event that may be in the same or different

segments or both. Furthermore its resolution is not limited to the density of the basis points since it can place an interaction in any location described by interpolation of neighbouring points. Additionally, a simple best-match fitting was also used in some parts of the work as a cross-reference of the results. In this case, a measured pulse is simply compared to all basis pulses using a χ^2 criterion and the best matching basis point is assigned as the interaction location. This method has only been used with single-segment events.

3.4 The matrix method: in-depth

We begin by creating a database of detector responses to single-point interactions along a grid of locations throughout the detector - this is the **basis set** and these locations are the **basis points** (likewise - a **basis grid**). A part of this database where only pulses from basis points located within one segment is a **segment basis set**. For a given interaction it is convenient to collect the waveforms from all relevant segments in a single vector called a **meta-signal** (fig. 3.4 for example). In this work, the meta-signals for the basis points were stored in the columns, m, of the matrix M (eq. 3.1).

$$\overline{s} = \overline{m}_1 x_1 + \overline{m}_2 x_2 + \cdots + \overline{m}_n x_n = M\overline{x} \tag{3.2}$$

All experimental signals $\overline{s}$ will be fitted with linear combinations of the basis signals. Unlike many other methods, the result of the fit is not a single point but a set whose basis signals combine to give the best match to the measured signal. Clusters of close-lying basis points represent a single interaction whose energy is the sum of the energies at the basis points and the position is the average of the basis point positions weighted with the assigned energies. This is possible because pulse shapes change gradually as the interaction position is varied – i.e. without discontinuities. The procedure thus provides a significantly greater granularity then that given by the density of the basis points. It must be noted, however, that the identification of basis points belonging to the same cluster is far from trivial. This is, however, only an issue for points within the same segment - those in different segments are clearly separated since the energy measured by each segment is known. Furthermore, there may be more than one combination of basis pulses which may give an adequate fit, the presence of noise making it impossible to guarantee that any one is the correct solution.

3.4.1 Solving the matrix equation

To solve eq. 3.1, the matrix M must be inverted; alternatively, Gaussian elimination may be used. The result is the best fit in the least square sense. Generally, however, the resulting vector $\overline{x}$ will contain any real values including negative ones. To avoid such non-physical solutions, the non-negative least square algorithm (NNLSA) was used [42, 43]. The algorithm is an iterative procedure that finds one positive element

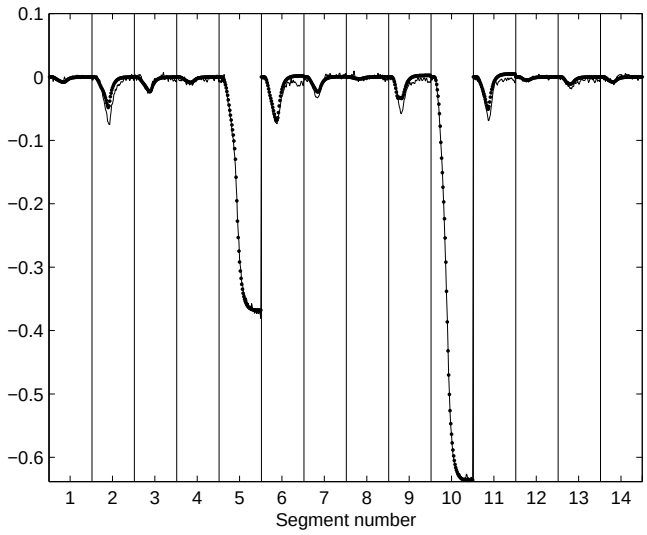

Figure 3.4: An experimental meta-signal (solid line) fit by the matrix algorithm (dots)

of $\overline{x}$ at a time and stops when a given tolerance is reached. Hence the condition that the number of non-zero energy deposits must be relatively low is also fulfilled by the algorithm. The Matlab [44] implementation of the algorithm was used. In general, the matrix M will have the number of columns equal to the total number of basis points in the detector, while the number of rows will be the number of samples of the pulse times the number of segments. The following parameters help to reduce the size of the matrix.[2]

- **number of waveform samples** The waveform should be well represented, but it is unnecessary to have a sampling frequency that much exceeds the typical frequency components in the signals. The length of the waveform needs to be such that it covers the entire charge collection time as well as some extra samples before and after needed to accommodate pulses that may be shifted by the timing algorithm.
- **number of basis points used** Only the basis sets for the segments that actually measured non-zero energy need to be considered. It is practical to

[2] As an example, in the 25-pixel $50 \times 50 \times 20$ mm detector where each segment has a 5-by-5-by-10 point grid, with 25 data points for each wave form, M would be a 6250-by-625 matrix. Without data reduction, the solution time would be on the order of tens of seconds - unacceptably slow even for off-line analysis.

calculate the basis sets for each segment and allow the algorithm to choose the right matrix.

- **number of segments in a meta-signal** The segments far away from the interaction points only receive vanishing transient signals. It is sufficient to use only the immediate neighbours of the hit segment (an exception would be a strip detector with narrow contacts where next-to-adjacent strips show significant signals).
- **number of non-zero singular values** The matrix M is in practice rank-deficient. Performing singular value decomposition, one finds that singular values decrease rapidly, and it has been shown in ref. [42], that setting the majority of singular values to zero while maintaining only a small number (typically 20), not only does not reduce the accuracy, but in fact improves performance in the presence of noise.

We begin with eq. 3.1. If the number of basis points in a segment is n and the number of samples in the entire meta-signal is l and $M[l \times n]$ is an l-times-n matrix,

$$M[l \times n]\, \overline{x}[n \times 1] = \overline{s}[l \times 1] \tag{3.3}$$

Performing singular value decomposition of M one obtains

$$U[l \times l]\, W[l \times n]\, V^T[n \times n]\, \overline{x}[n \times 1] = \overline{s}[l \times 1] \tag{3.4}$$

where W is a diagonal (non-square) matrix with the singular values placed along the diagonal ordered from greatest to smallest[3]. Setting all but the k greatest singular values to zero allows to discard large parts of the matrices, effectively reducing dimensions from n and l to k (note that the dimensions of the measured signal, $\overline{s}$, and the energy deposit distribution in the detector, $\overline{x}$, are unchanged). With this truncation we obtain

$$U[l \times k] W[k \times k]\, V^T[k \times n]\, \overline{x}[n \times 1] = \overline{s}[l \times 1] \tag{3.5}$$

$$W[k \times k]\, V^T[k \times n]\, \overline{x}[n \times 1] = U^{-1}[k \times l]\, \overline{s}[l \times 1] \tag{3.6}$$

$$(WV^T)[k \times n]\, \overline{x}[n \times 1] = U^{-1}[k \times l]\, \overline{s}[l \times 1] \tag{3.7}$$

where U^{-1} is the pseudo-inverse of the matrix U. For a given basis matrix, M, the matrices in eq. 3.7 are constant regardless of the input data. This suggests that these matrices may be computed in advance and stored in the memory. In this work, the segment basis matrices, M, the matrices WV^T and U^{-1} were calculated

[3] it is always possible to choose any order of singular values along the diagonal of W by reordering rows and columns of U and V

for every segment as well as for every combination of two segments for the detector geometries studied. Thus the solution requires a multiplication of U^{-1} by $\overline{s}$ followed by the solution of

$$(WV^T)[k \times n]\,\overline{x}[n \times 1] = (U^{-1}\overline{s})[k \times 1] \tag{3.8}$$

using the non-negative least square algorithm. The events with more than two triggered segments must be treated in a different way, since it is unrealistic to have the matrices for all possible segment combinations in memory. While it may seem reasonable to perform the procedure in eq. 3.3-3.8 for a matrix M containing the entire detector basis, note that the total number of basis points n is not reduced in the last equation. This creates a very large system for the NNLSA, and it was found that it is faster to assemble the basis matrix with the necessary segments only, do the singular value decomposition and solve the system on an event-by-event basis. Fortunately, such events are quite rare and did not limit the overall speed of the analysis.

3.4.2 The definition of the interaction points

The output of the matrix method is the vector $\overline{x}$. Each element, x_i is the assigned deposited energy to the basis point i. The linear combination of all the basis signals, $\overline{m_i}$, given by

$$\sum_{i>0} x_i \overline{m_i} \tag{3.9}$$

provides a fit to the measured pulse, see fig. 3.4. Fig. 3.5 shows the energy assigned to the basis points for the same event. An interaction point may be defined as the average position weighted with the assigned energy, in other words the center of mass of the points within one segment. This procedure works well if there indeed was only one interaction in the segment. In the case of multiple interactions, it finds the center of mass of the interaction points. Nevertheless, this procedure was used in the analysis presented in this work. Fortunately, the segments of planar detectors tend to be relatively small (compared to detectors such as those of AGATA), and the events with multiple interactions per segment are in the minority.

In order to understand the difficulty of resolving multiple interactions in a segment, let us consider the sets of basis points returned by the matrix algorithm. Figure 3.6 shows a reconstruction of a single interaction close to the lower left corner of the segment. The basis points chosen for the fit include some at the opposite edges of the segment. Note that this is actually a very good fit in terms of position resolution, however if one was to attempt to find clusters of basis points and define more than one interaction, it is likely that this event would be misinterpreted as a multiple interaction.

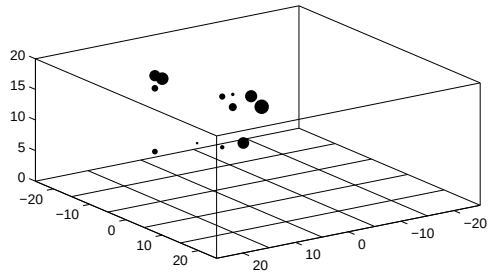

Figure 3.5: The basis points contributing to the fit in figure 3.4. The areas of the dots represent the assigned energy.

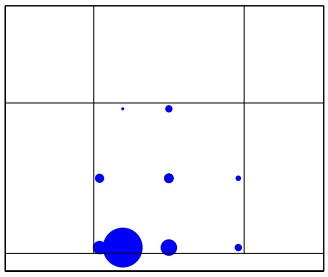

Figure 3.6: The basis points assigned to a single interaction are often spread out over a segment.

3.4.3 Resolving multiple interactions

There is a number of ways to approach the problem of two or more interactions in a segment. As discussed above, a major problem is the misidentification of single interaction events as multiple ones. It has been suggested that with an a priori knowledge of the number of points, provided by an additional algorithm, it may be possible to identify multiple interaction points successfully [45]. This can be determined through the analysis of the net charge signal. A charge signal is composed of the sum of two components of generally different duration induced by holes and electrons. A net signal therefore typically consists of two segments with a visible [4] change in the derivative where one of the charge species is collected and stops contributing to the signal. When more than one interaction is present additional changes in the derivative may be found. This method can thus distinguish pulses caused by two or more interactions, provided that the interactions are at different depths and that the noise level is sufficiently low. If a multiple interaction is identified in this way, an attempt to arrange the output points of the PSA into several clusters can be made.

Alternatively, one can begin the analysis with the assumption that there are two interactions. If at the end of the fitting either the quality of the fit is too poor or the resulting two clusters are not sufficiently separated, the algorithm then should merge all points into one. A method based on this idea was tested with the 16-fold segmented clover detector model. The algorithm searched for two well-separated point deposits in $\overline{x}$ with large assigned energies. The fitting procedure was then repeated using only small clusters of basis points in the vicinities of the two locations. If this new solution presented a good fit to the measured signal, the event would be reconstructed as a double interaction. This is illustrated in figure 3.7.

When using simulated data with double or single interactions in only one segment, this method could successfully identify 2/3 of the double interactions, however it also misinterpreted 1/3 of the single interactions as double. Of the correctly identified double interactions, only in half of the events were the energies and positions of both estimated correctly. A general problem encountered when resolving more than one interaction in the same segment is the determination of the interaction energies. The energy deposit in a segment of a germanium detector is deduced by applying a moving window deconvolution (MWD) algorithm in case of a digital sampling data acquisition system (see appendix A) or by a shaping amplifier in case of an analogue one. In each case, the preamplifier signals are integrated for several μs – a much longer time than is typically available in a sampled pulse shape. For two interactions, the well-known total segment energy needs to be partitioned. Here the good resolution of a germanium detector is lost because the information about the properties of the individual interactions is only present in the few ADC samples corresponding to the rising edge of the pulse. For the events where double

[4] Visible, provided that the preamplifier response is sufficiently fast.

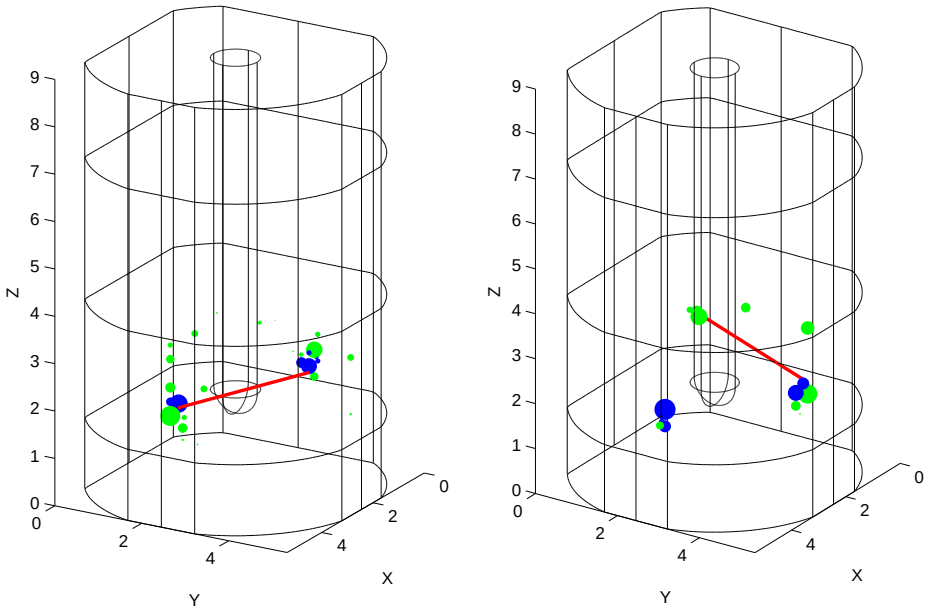

Figure 3.7: Performance of the algorithm for resolving double interactions. A successful identification is shown on the left and one where one of the points is not located correctly on the right. Here the green points are the solution, $\overline{x}$, where the entire segment basis is used. The blue points show the final solutions using only basis points in the vicinity of the two estimated clusters. The ends of the red line indicate the real interaction locations.

interactions were both correctly identified as well as correctly located, the energy resolution of the individual deposits was approximately 40 keV with interaction energy ratios between 1:1 and 1:3 (with the higher energy interaction of 600 keV). The situation is expected to deteriorate further if additional interactions are present in other segments or if the two interactions in the same segment have very different energies.

Chapter 4

Experimental applications

This chapter presents the applications of pulse shape analysis and related methods for segmented germanium detectors. Measured pulses were available from the KTH planar, SmartPET planar and TIGRESS clover detectors. Detector simulations have been made in each case and PSA reconstruction performed using both measured and simulated pulses, this is summarised in section 4.1. The the findings of these analyses are discussed in section 4.2. In sections 4.3 and 4.4 effects specific to detector edges and crosstalk in segmented detectors are discussed. Summaries of two experiments performed with the KTH 25-pixel planar detector – Compton imaging (paper 1) and Compton polarimetry (paper 2) measurements – are presented in sections 4.5 and 4.6. The pulse shape analysis method described in chapter 3 was used in both experiments. In each case, it was necessary to reconstruct events with two interactions – one Compton scattering and one photo-absorption. In practice, this implies the selection of events where two segments were triggered with the total energy equal to that of the γ-ray of interest. Such selection does not, of course guarantee that there are not more than two interactions – multiple interactions within each or either of the triggered segments are possible. In some cases, however, it is possible to suppress the contribution of such events.

4.1 Pulse shape validation

The set of basis signals required for PSA needs to be calculated. Pulse shapes measured when scanning a detector can be used as a validation, as could data obtained in other types of measurements. Generally, signals from a scanned detector will represent averages over a volume a few mm across due to the size of the collimators and the extent of the source [1]. Furthermore, a scan of a large-volume germanium detector takes a very long time – about 3 weeks for an AGATA detector where only 6 horizontal slices are measured (only one per segment) [46]. For an array such as AGATA, a scan of each detector is very time-consuming. At the same time, detectors will differ because the impurity concentration and rotation angle of the crystal

axes can vary from crystal to crystal. Furthermore, in AGATA, the three different detector geometries will not show identical pulse shapes. Therefore, pulse shape calculations must be accurate and well understood in order to reliably describe all detectors.

The detectors for which measurements have been compared to simulations in this work – the KTH planar pixel planar detector, the SmartPET (in the University of Liverpool) planar double-sided strip detector and the 8-fold segmented TIGRESS (in TRIUMF) clover crystals – are described in sections 2.4.1 and 2.4.2. For each detector, a simulation was created and the resulting pulse shapes were compared to measured data. Such analysis is needed in order to gauge the accuracy of the simulation as well as to identify the possible sources of discrepancies and their potential importance. These three types of detectors are each of the type that are considered for the future DESPEC array described in chapter 5.

In addition to the data used in the imaging and polarization measurements described later in this chapter, a number of pulse shape measurements with the KTH detector have been analysed in order to test the validity of the calculated pulses. These included tests with ^{241}Am (59.5 keV), convenient when testing the response to interactions close to the surface and ^{133}Ba and ^{137}Cs for photons of around 300 and 662 keV, respectively, that easily penetrate to any depth into the crystal and result in signals of larger amplitude. While no automatic scanning set-up is available at KTH, a handful of points were measured manually using lead collimators as described in ref. [1]. Also measurements without collimators, where an entire detector is illuminated, were used. Additionally, several measurements with the SmartPET and TIGRESS detectors were made available for the comparison with the simulation methods used in this work. These included singles scans with the 662 keV line of a ^{137}Cs source, as well as a coincidence scan (see section 2.7) of the TIGRESS detector.

When using data from a singles scan or from a measurement with an uncollimated source, interaction positions are not known on an event-by-event basis. Nevertheless, it is possible to gauge the performance of a PSA reconstruction by studying the distribution of reconstructed locations. Unfortunately one cannot select single-site interaction events in such measurements with the same certainty as in the case of a coincidence scan. For energies above $\sim$150 keV, photopeak events will usually consist of more than one interaction even if one-segment events are selected. PSA reconstruction of such events using the matrix algorithm (or any method that merges all interaction locations in a given segment into one), is expected to return positions concentrated in the middle of segments, since generally a centre of energy of a number of interactions is located somewhere between the real locations. A measurement using a low-energy γ line, such as 59.5 keV in ^{241}Am, results in predominantly one-interaction events, however, the vast majority of these will be at the very surface of the detector. Signals of this energy are also significantly more difficult to analyse since in many cases the amplitude of the transient pulses is close to the noise level. Another possibility is to use backscattering events, where a 662 keV photon scatters at an angle close to 180° and then escapes from

the detector. In this case, single-segment interactions with an energy deposit of just below 477 keV are selected. This favours single-site interactions to a much greater extent than the selection of photopeak events, however, with a narrow gate around the Compton edge, the event rate also tends to be much lower.

4.2 Systematic errors

Many types of discrepancies between the PSA basis and measured pulses can contribute errors in position reconstruction. The issues presented in this section were investigated using either simulated or measured single-segment events.

A significant level of white noise, while affecting all parts of the signal equally, has a general tendency to force the reconstruction algorithm to preferentially use a particular part of a segment volume to place the reconstructed interaction locations. An example of this is shown in fig. 4.1 for the clover detector. For clarity a 2-dimensional projection of reconstructed interaction points is shown for two noise levels. Simulated data was used here, ensuring that no discrepancies other than noise are present.

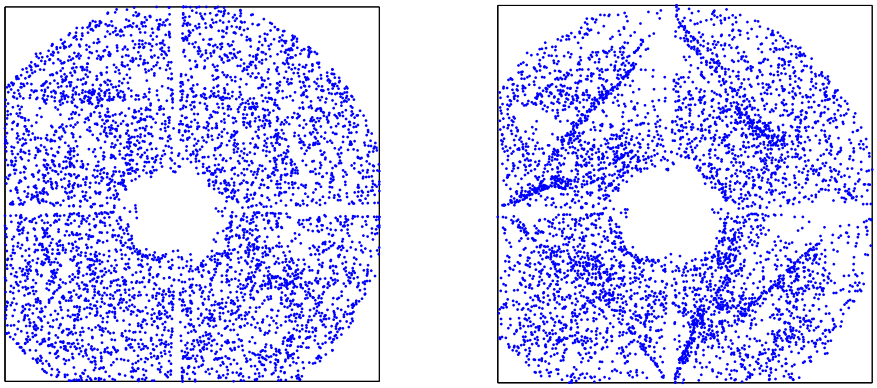

Figure 4.1: Reconstructed randomly placed interactions in the 15–25–30–20 clover detector. An x-y projection of the points in the third segment ring of the detector are shown. **Left:** no noise, **right:** 12.5 keV noise (×5 the noise level used in the simulations in chapter 5).

As already mentioned in section 3.2, an error in time alignment of the measured pulses with respect to the basis set can cause large errors in reconstruction. Interestingly, for the clover detector, a redistribution of reconstructed points very similar to that shown in fig. 4.1 occurs if a systematic time shift is present, even with no

noise. This suggests that the addition of noise primarily injects the error through the inaccuracy in timing. Generally, timing misalignments between the measured pulses and the basis set result in large discrepancies in the leading edge of the net charge pulse. This results in the selection of basis pulses from the wrong depth, or the wrong position along the trajectory of a charge – in extreme cases selecting the pulses with the highest or lowest rise time available – i.e. moving the interaction point closer to one or the other contact than it should be. Such a displacement, on the other hand, increases the error in the transient pulses, since the amplitude and the polarity of these typically vary with the depth while the amplitude also varies with the proximity to the net charge segment. Therefore an overall shift towards or away from a contact surface is usually accompanied by a shift in the transverse direction as well. This effect is clearly visible in fig. 4.2 a) (and to a lesser extent b)) where a shift the lateral position also causes a reordering in the lateral coordinates. The grouping of reconstructed points in the clover detector in fig. 4.1 is in fact a very similar effect. There the points are shifted somewhat in the radial coordinate, however, the strong visible agglomeration of points comes primarily from a shift in the angular coordinate, away from the segmentation boundary.

A similar effect can be observed in reconstruction if the total charge transport time is incorrect – which may be the case if wrong impurity concentration, crystal orientation, or bias voltage is used. Similarly to a timing error, the apparent deviation here is also due to the difference in the rise time of the net signal. In such situations, it was found that a better position reconstruction occurs if only signals from one side of the detector are used – for example the pixel signals of the KTH detector, but not the full energy signal. This may sound counter-intuitive, however, the reconstruction algorithm appears to more easily compensate for for an error in one of the net charge signals by shifting the reconstructed point slightly. This, however, may cause an even larger discrepancy with the opposing net charge signal that will shift the point even more. Examples of this are shown in 4.2.

During the experiments presented later in this chapter and in papers 1 and 2, the anode signal of the KTH planar detector was *not used* due to technical problems with the readout of the anode preamplifier. The effects presented above were discovered later once the anode signal could be used again. While no large uncertainties are expected for this detector in terms of the impurity concentration, or charge mobility properties, the exact response of the preamplifiers was not known. There are usually differences in the readout of the two sides of the detector. Since one side is grounded and the other held at the high voltage potential, the preamplifiers must be connected differently – DC-coupled on one side and AC-coupled on the other. The preamplifiers themselves are usually of a different model for the core/full energy contact and for the segments. Due to this, preamplifier response functions and rise times can be different for the two sides of the detector. In the case of the KTH detector, the reconstruction using the anode signal required a significantly faster preamplifier response folded into the basis set for the anode pulse shape.

The anode signal, while not necessarily included in the fitting procedure, was

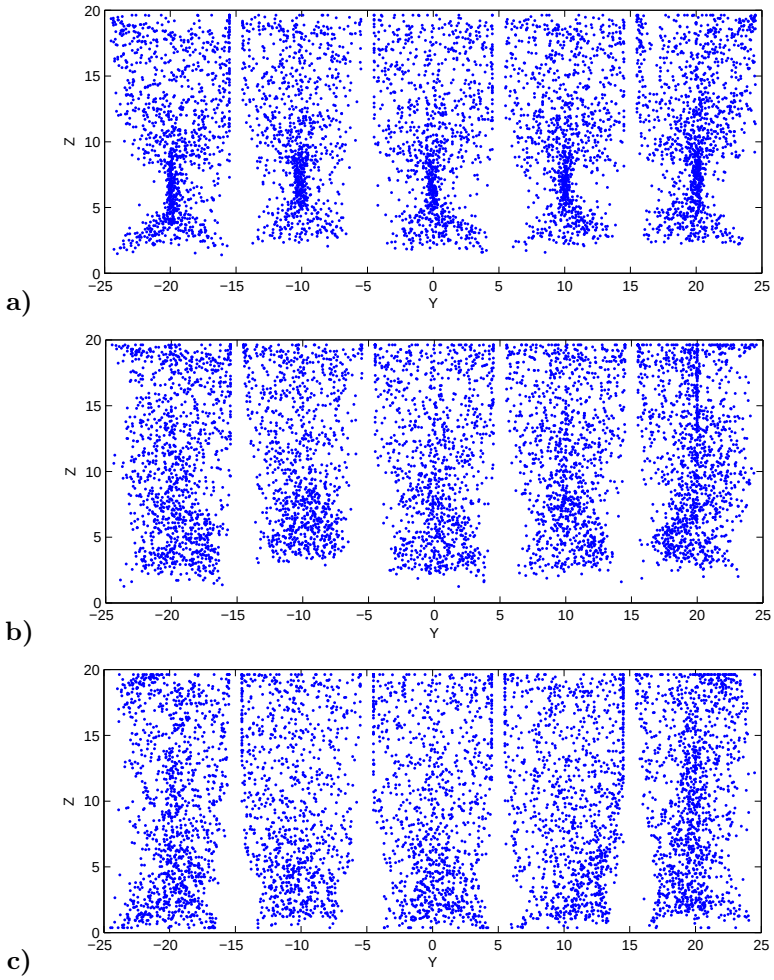

Figure 4.2: y-z projection of reconstructed measured interactions of the 303 keV photons in segments 16 through 20 of the KTH planar pixel detector. **a)** reconstruction using the same preamplifier rise times and delays for the segments and the anode; **b)** same as above, but without the anode signal; **c)** preamplifier rise times set to 30 ns for the anode and 60 ns for the pixels.

in some cases used for timing. Signals such as shown in fig. 3.3 can be obtained from either summation of the pixels, or using the full energy contact (this is the case in the figure). In experiments it proved more reliable to use the single anode signal, since summation of 25 pixels results in a greatly amplified pick-up noise (this type of noise tends to occur synchronously in all channels) which was often present during the measurements.

Similar effects were observed in the analysis of the SmartPET data. Here, however, it is quite inconvenient to remove a net charge signal from one of the sides, since it is not found in the same channel from one event to the other (performing this *did* result in an effect similar to the case of the pixel detector). It was also found that the problem could be partially solved by making an adjustment to charge mobilities, thus directly affecting the signal rise times. However, no apparent physical ground for such an adjustment seems to exist.

4.3 Edge effects in planar detectors

The electric field lines and, consequently, charge drift trajectories are very nearly straight in the central region of a planar detector. Closer to the passivated surfaces at the edges, the field lines become distorted due to the presence of a typically conductive cryostat material close to these surfaces. This effect seems to be quite weak in the KTH planar detector (fig. 4.3, left) since the edges of the crystal are rather far from the aluminium wall of the cryostat, ~ 2 cm, furthermore the cathode side is essentially uniformly held at ground potential (except the 300 μm gaps), making the electric field distribution nearly symmetric. This is consistent with the electric field simulations in ref. [47].

Additionally, any trapped charge at the surfaces will further modify the field distribution. As shown in fig. 4.3, for the KTH pixel detector a significantly better charge collection occurs if the surface charge is positive. The effect of the surface charge on trajectories is not symmetric with respect to the two charge species since the electric field is strong on one side of the detector and weak on the other. In this detector electrons drift primarily through the strong field and therefore suffer less deflection due to a surface charge, whereas holes, whose drift takes place mainly in the lower-field side of the detector are deflected more easily (assuming that the surface charge density is constant).

Since in the region close to the edge of a planar crystal a part of the charge may become trapped at the surfaces rather than collected at a detector contact, the energy measurement will be incomplete. The contribution of such events is prevented by, an additional electrical contact, known as a guard ring, which is placed at the edge of the detector, as shown in the top part of fig. 4.3. A guard ring is held at the same potential as the contact it encloses, i.e. at ground potential in the case of the pixels of the KTH planar detector. The germanium volume from which part of the charge is lost is usually referred to as a dead zone and exists in all planar detectors. Due to this, the guard ring cannot be made arbitrarily narrow,

but should be optimized so that excessive detector volume is not rejected. A guard ring also prevents a contribution of surface leakage currents to the signals of the detector contacts.

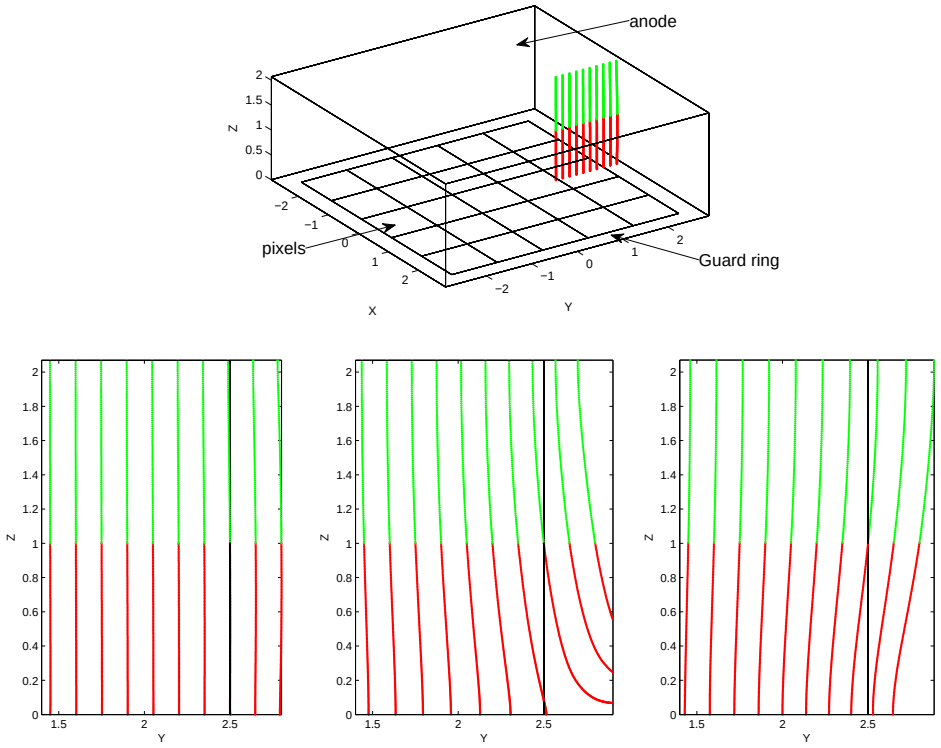

Figure 4.3: Charge drift trajectories (red – h^+, green – e^-) in the presence of a surface charge. **Left:** no surface charge; **middle:** negative; **right**: positive surface charge. The segmented cathode is the bottom surface at $z = 0$. The electric field is strong near the anode at the top of the diagrams. The guard ring starts at $y = 2.5$. The surface charge used here is $5 \cdot 10^{-6}\, C/m^2$ [47].

While no direct method to test the surface charge properties was available, the situation is likely similar to that corresponding to a positive surface charge. This is because the efficiency of the outer segments was found to be 10-15% higher, and somewhat higher still for the corner segments[1], indicating that these collect a fraction of interactions that occur in the volume subtended by the guard ring. Had the surface charge instead been negative, charges from parts of the outer segments

[1]Measured at the energies of 276-384 keV of the ^{133}Ba source.

would be collected on the guard ring, or indeed be trapped on the crystal surface, reducing the efficiency of those segments. Similar effects are expected at the back surface of a coaxial detector, however, due to the typical depths of coaxial detectors, fewer γ-ray interactions occur in this region and it has not been studied equally well. The total dead volume is significantly smaller than in a planar detector if the charge polarity is such that the dead volume is concentrated around the inner contact.

4.4 Crosstalk

Crosstalk is the influence of a signal in one channel on all or any of the other channels. It exists in all segmented detectors to one degree or another. The term *crosstalk* is usually associated with unintended interdependence between various electronic components, such as the segment preamplifiers or the inputs of a digitizer. In segmented detectors, effects that manifest themselves in the same way as electronic crosstalk also originate in the segmented crystal itself due to capacitive couplings from segment to segment (and in particular full-energy contact to segment), segment to ground and the capacitances of AC-coupled preamplifiers [48].

In the following, the combined effect of crosstalk in the crystal and in the electronics is considered. It can be divided into two components. Proportional (or integral crosstalk) is the component that contributes with an induced net charge and is proportional to the deposited energy. Derivative crosstalk is a transient component that is only present during the charge collection and is proportional to the time derivative of the charges induced on the contacts.

Proportional crosstalk

Proportional crosstalk results in shifts in segment energies when other segments are hit. Fig. 4.4 a) shows the average effect of an interaction in one of the segments on the signals in all other segments of the KTH pixel detector. Fig. 4.4 b) and c) show examples of pulses contributing to the average in a). An average of 500 signals originating from arbitrary locations within the segment is shown. Therefore, since various shapes of the transient signals are present in the interaction-free segments, the average transient pulse shape does not necessarily represent any realistic pulse shape. Nevertheless, after the time corresponding to the maximum charge collection time, the transient signals should return to a zero base line. A shift in the base line present for later parts of the pulses is equivalent to an apparent net signal, which causes a non-zero energy value in a digital or analogue readout system.

Proportional crosstalk has little effect on the rising edge of a pulse and on the transient pulses. PSA is rather insensitive to the amplitude of net pulses and since only the transient parts of the pulses are used for PSA, proportional crosstalk does not seriously affect position reconstruction. Note that since the pulses shown in fig. 4.4 a) are averages of positive, negative and bipolar transient pulses, their

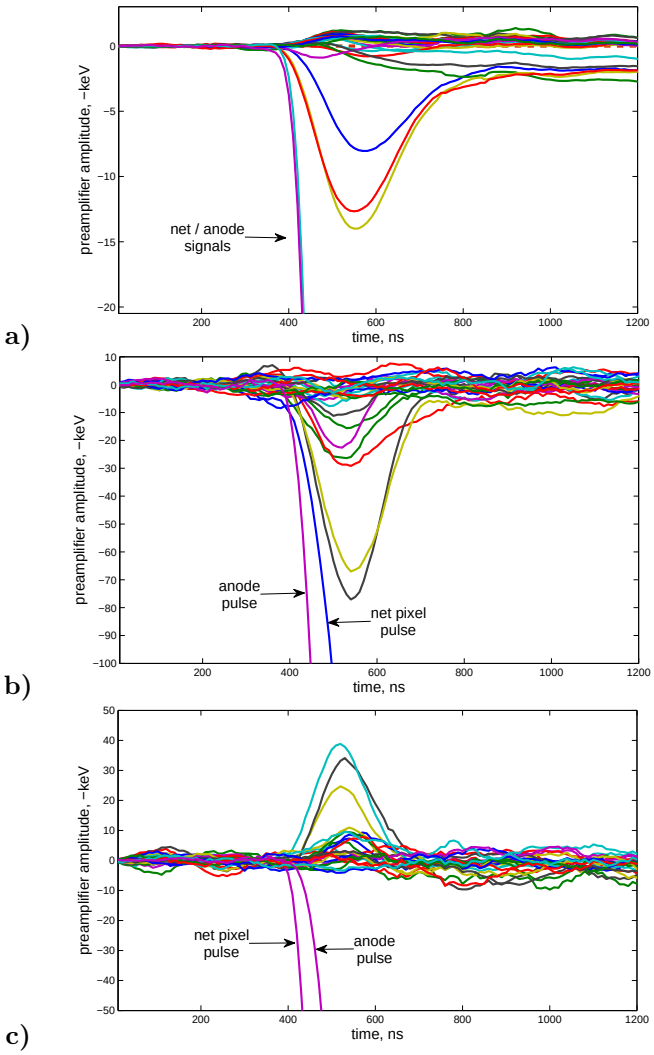

Figure 4.4: **a):** average of 500 pulses for interactions of 477 keV in a corner pixel of the KTH detector. The apparent net components in the segments other than the target segment are clearly visible after the transient pulses have ended (times >800 ns). These result in a non-zero energy value in the readout system and correspond to proportional crosstalk. **b, c):** single events from the same data set with positive and negative transient pulses. Note the difference in the vertical scale. The amplitudes of the net signals are ≈-477 keV.

amplitudes are greatly reduced relative to the following offsets due to crosstalk, as compared to the pulse shapes from the single event examples shown in fig. 4.4 b), c).

Proportional crosstalk correction for the KTH pixel detector

For events of fold 2 or higher, where a photon is absorbed in more than one segment, summing the segment energies results in a total energy that deviates from an equal energy deposit in a fold 1 event, when only one segment is hit. This is caused by proportional crosstalk – energy deposit in each segment results in a shift in energy in other segments. This is illustrated in fig. 4.5, where the 662 keV peak of a ^{137}Cs source is shown for fold 1, 2, 3 and 4 events. The peak is shifted somewhat towards higher energies when it's energy is calculated by summing over the hit segments. Using the full energy anode contact readout, peak position is independent of fold.

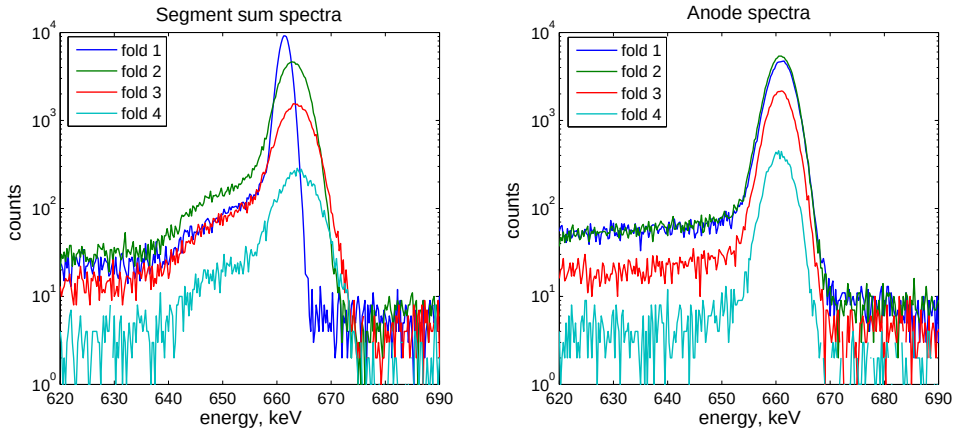

Figure 4.5: **Left:** energy spectra of a ^{137}Cs obtained by summation over up to 4 hit segments. **Right:** anode spectra for the same events.

Fig. 4.6 shows the measured effect of crosstalk in fold 1 photopeak 662 keV events. When the photon is fully absorbed within one segment, the energy values recorded by the digitization system should ideally be zero in all other segments. However, well-defined non-zero average values are observed, which may be positive or negative.

The position of the peaks is correct for one-segment events, since energy calibration is normally performed for this type of events. For fold 2 and higher events, it is necessary to correct for proportional crosstalk. To achieve this, a 25×25 matrix, C was constructed where an element, C_{ij} is the energy measured in segment j when segment i absorbs an energy of 1 MeV. This matrix, for the KTH detector, is shown in fig. 4.6. Let E be a vector containing the measured energies, E_k, of triggered segments, k. The corrected energies, Ec, are then given by the

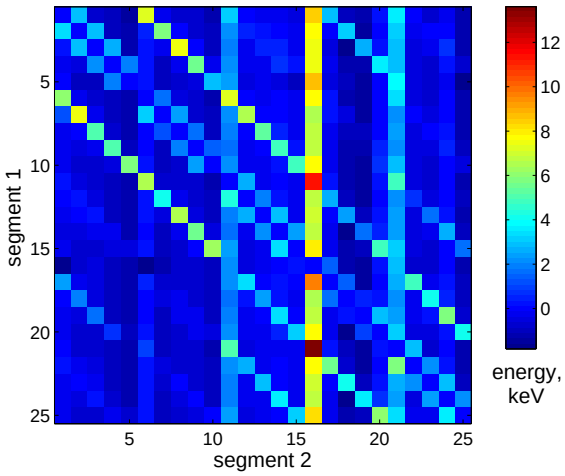

Figure 4.6: Proportional crosstalk measured in the KTH pixel detector. The map indicates the energy measured in segment 2 when segment 1 detects a 1 MeV photon. The crosstalk between the neighbouring pixels can be seen in the form of the diagonal lines. Large values are found in some channels (16 in particular) in response to a detection in any other segment. These channels may be influenced by the full energy signal, possibly due to the layout of the preamplifier board.

product of E and $(1 - C)$. The corrected energies in triggered segments, Ec_k, are then used in the data analysis, while segments where no interaction took place are discarded[2]. In a fold 2 event, where energies E_a and E_b are detected in segments a and b, this is equivalent to setting the corrected energies to $Ec_a = E_a - E_b \cdot C_{ba}$ and $Ec_b = E_b - E_a \cdot C_{ab}$.

Fig. 4.7 shows the segment sum spectra after this correction. The resulting peaks are now at the same position. The energy resolution is worse for events of fold 2 and higher due to the summation of the noise componets from several signals. It is possible to somewhat improve it by combining the information from the segments and the full-energy contact [48].

This crosstalk correction method relies on the energy measurement very close to zero. In a typical energy calibration a number of photon energies from standard sources are used, such as ^{133}Ba or ^{152}Eu, with lowest energies of 81 and 122 keV respectively. Calibration at very low energies can be unreliable, and in general there will be a non-zero constant offset. For the purposes of the crosstalk correction as

[2]This operation can be seen as a first-order correction, since the charges induced by crosstalk will in turn generate further offsets. Since the amplitudes of the proportional crosstalk signals tend to be well below 1% of the true net signal, further corrections have been omitted here.

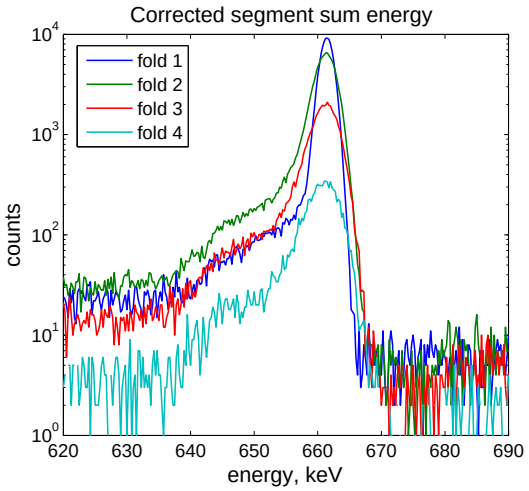

Figure 4.7: Energy spectra of a ^{137}Cs obtained by summation over up to 4 hit segments after crosstalk correction.

described above, the effects of the constant offset should be removed, while the linear (and higher order, if used) gain coefficients should be kept when determining the energy in a segment that has collected no real energy deposit. If this is not done, the true zero energy, and hence the elements of C would be shifted by the value of the constant offset. This complication is avoided in the method described in ref. [49], where crosstalk between a pair of segments is measured as the difference between energies in fold 1 and fold 2 events. However, very large statistics are required in order to obtain enough events from distant segments. Another option is to determine the elements C_{ij} directly from the amplitudes of the offsets in the preamplifier signals (see fig. 4.4).

Derivative crosstalk

Derivative crosstalk is proportional to the time differential of a signal and therefore describes the *transient* crosstalk components induced by the changes of a signal in another channel. The resulting effect is very similar to the creation of transient charge pulses in a segmented detector and occurs during exactly the same time. Due to this, it was not possible to disentangle the derivative crosstalk from the transient pulses in measurements performed here. It likely constitutes a major part of the discrepancies between simulated and measured signals.

In order to measure derivative crosstalk, it is necessary to utilize the fact that the transient signals due to crosstalk are caused by charges induced on conducting electrical contacts and, unlike transient charge pulses, are independent of the

interaction location and charge drift trajectories. A method for experimentally determining derivative crosstalk based on this premise is described in ref. [50]. If single interactions very close to the boundary of two segments (A and B) are measured, where some result in a net signal in segment A and others in segment B, the transient pulses from all remaining segments will be virtually identical, since their sensitivity to the small difference in the position of the interaction is vanishing. The differences in the transient signals for segments other than A and B between events where charge collection occurs in segment A or B will then be due to derivative crosstalk. A complete database of crosstalk signals can then be obtained by performing this measurement for every combination of neighbouring segments A and B.

4.5 Compton Imaging

The concept of Compton imaging relies on the relationship between the energy transferred to an electron in a Compton scattering event to the angle between the directions of the incoming and the outgoing photons. This relationship is given by the formula

$$E_{e^-} = \frac{\frac{E_\gamma^2}{m_e c^2}(1-\cos\theta)}{1+\frac{E_\gamma}{m_e c^2}(1-\cos\theta)} \tag{4.1}$$

While the scattering angle θ is determined by the energy values, the remaining degree of freedom is given by the momentum vector of the recoiling electron. This cannot be measured in most solid state detectors. Thus the direction to the source of the γ-ray can be constrained to the surface of a cone with the vertex in the first scattering point, as in fig. 4.8. When the total energy of the γ ray is known, the angle θ is obtained using only the first two scattering points, or – in case of only one scattering – the Compton and the photo absorption points. This can be utilized if the photon can be assumed to be fully absorbed within the detector, or if the overwhelming part of the radiation is monoenergetic, as is the case in most medical applications where a single isotope, e.g. ^{99m}Tc, is used. In cases of incomplete energy collection, three scattering points are required in order to reconstruct a cone [51].

The ability to reconstruct the interaction points of a γ-ray to millimetre precision is of great value for Compton imaging. Without the use of pulse shape analysis, the position resolution is constrained to the physical size of the detectors or detector elements. As a result, a highly granular detector systems must be used. By contrast, a relatively compact single germanium detector with a 3d position sensitivity is capable of a 4π imaging. Alternatively, two, or more detectors can be used – some as scatterers and others as absorbers. The main fundamental limitation of Compton imaging is that the energy to angle relation in equation 4.1 is only correct when the momentum of the electron on which scattering takes place is negligible compared to E_{e^-}. Since electrons are bound in atoms, however, deviation in E_{e^-}, known

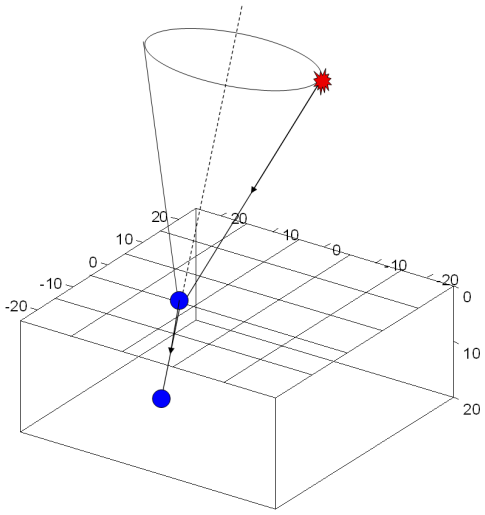

Figure 4.8: The concept of Compton imaging and the 25-pixel planar detector.

as the Compton profile [52], can be significant, especially for low photon energies. Another uncertainty in such a measurement is the range of the Compton electron, since it is its energy deposition and not the location of the Compton interaction that is reconstructed in a detector. Interestingly, the two above-mentioned effects on average counteract each other, resulting in an overall reduced error [1]. The electron range can also set limits on the minimal dimensions of a detector. While this is not a serious concern in a typical germanium detector, the electron range becomes much more critical in thin silicon detectors [53].

4.5.1 Summary of paper I: imaging with the planar HPGe detector

The imaging capability as well as the attainable position resolution were tested using the 25-fold segmented planar pixel detector. This experiment is described in detail in paper I. A ^{137}Cs source emitting 662 keV photons was used for the imaging tests. Images were reconstructed for a source placed 90 cm away from the detector, in one case along the normal direction to the cathode contact and in the other along the direction 45° off the normal to the cathode face.

This experiment was mainly aimed at the verification of the PSA technique. Experimental images were compared to those obtained in simulation, thereby providing an estimate of the experimental position resolution. In order to thoroughly test the PSA, it was decided to use only events with interactions in neighbouring pairs of segments, and only in the 9 inner segments. In this way, complex sig-

nals with superimposed pulses from more than one interaction were treated while ensuring that each interaction had a complete set of mirror signals available for PSA.

The image is reconstructed using cone back-projection. The cone from each interaction is projected onto a sphere enclosing the detector. The intersection of a cone with the sphere yields a circle. Figure 4.9 shows several cone projections, here one hemisphere is mapped onto a square similarly to a typical world map. Note that many cone projections are only partially visible as lines crossing the entire map. This is a consequence of the detector geometry – the requirement of two triggered segments has a tendency to favour events where the photon was scattered at an angle around 90°, thus the reconstructed cone is very wide, often intersecting both hemispheres. The cones close to the poles (at the top and bottom of the picture) are strongly distorted due to the map projection. A much larger number of projections contributes to the images for which angular resolution was determined as shown in the paper.

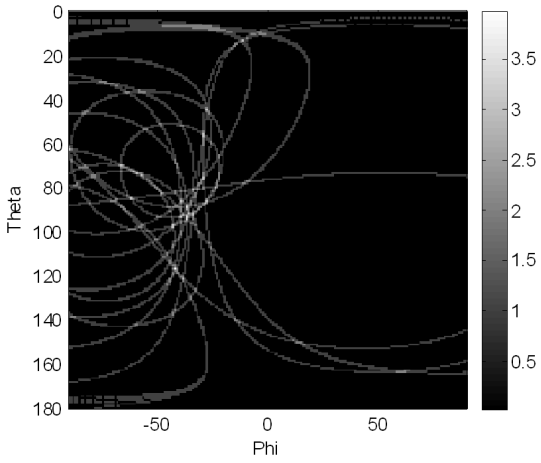

Figure 4.9: Back-projections of cones onto a map of one hemisphere.

A simulation of the experiment was performed in GEANT3 with the low energy Compton scattering (GLECS) package [54] and was compared to the experimental results. In the simulation, the position resolution for the interaction points was varied in order to find a corresponding point source image resolution equal to that obtained in the measurement. This position uncertainty was found to be 1.5 mm (std. dev.). Furthermore, the imaging efficiency of the set-up[3] was estimated through simulation to be 5.6%, taking into account the event selection criteria used

[3]defined as the fraction of the photons emitted into the solid angle of the segments used that are used for the image

in the measurement. This included segment combination selection, energy threshold set in the measurement and the effective merging of interaction points that occur in the same segment.

When dealing with events where only two interaction points are detected, γ-ray tracking reduces to only two options. In imaging, the position or distribution of the source, naturally, is an unknown. The total energy, however, can in many applications, such as medical imaging, be assumed to be fixed; therefore full absorption events can be identified, and both E_γ and E_{e^-} are known. With only these constraints, it is not possible to determine which of the two points is the first interaction. According to the simulation, however, in the majority of the events, the larger energy deposit is at the first interaction point for the geometry of the KTH detector and the photon energy of 662 keV. The tracking strategy needs to be determined individually for any Compton imaging set-up. It will depend on the photon energy (and assumptions of whether it is known a priori), number of interactions located per event and the position and geometry of the detector(s). A detailed Monte Carlo analysis of these aspects is presented in [53], where in particular an imaging detector consisting of a stack of thin silicon detectors is investigated.

This experiment demonstrated the possibility of evaluating the precision of PSA position reconstruction where a lengthy scanning procedure can be avoided. Conventionally data from a scanned detector would be compared to a simulated database of detector signals. The advantage of this technique is that the interaction location can be chosen freely. On the other hand, while using imaging, the reconstructed data naturally includes events with more than one interaction point, as is the case for the majority of γ-ray events in a germanium detector. Position resolution for multiple interaction events is in practice worse than for single-site interactions (such as those selected when scanning a detector). A comparable method for evaluation of position resolution relies on the analysis of Doppler correction in an in-beam experiment such as the test runs with the AGATA demonstrator [15, 16], where an experimental line width after Doppler correction is compared to a simulated one and position resolution in simulation adjusted accordingly.

The efficiency of 5.6% is high for a Compton imaging device, while the obtained angular resolution of 30° is rather poor. As a comparison, in a similar experiment using a coaxial segmented detector [18] only non-neighboring segments were used, resulting in an efficiency of an order of magnitude lower (0.4%), while significantly increasing the image resolution (to 5°). This difference is expected due to the better definition of the cone axis when the interaction points at a large separation are selected. For the planar detector used in this study it was found from the simulation that image reconstruction, where the hit segments are required to be separated by one segment, enhances the angular resolution of the image by a factor of 2.3 while lowering the efficiency by a factor of 3.5[4]. The combination of all

[4]The pixels of the planar detector are smaller than the segments of the coaxial detector used in ref. [18], so demanding 1-segment separation leads to smaller distances between interaction points.

possible segment combinations would of course maximize the efficiency, as well as improving the image resolution as compared to data from adjacent segments only.

4.6 γ-ray polarimetry

Compton scattering can be used to measure the polarization of a beam of γ photons. A comprehensive review of the Compton polarimetry techniques can be found in [55]. The Compton scattering angle, θ, is defined as the angle between the directions of the incoming and the outgoing photons. The azimuthal scattering angle, ϕ, is defined as the angle between the polarization vector of the incoming photon and the plane spanned by the incoming and outgoing photons' momentum vectors, see fig 4.10.

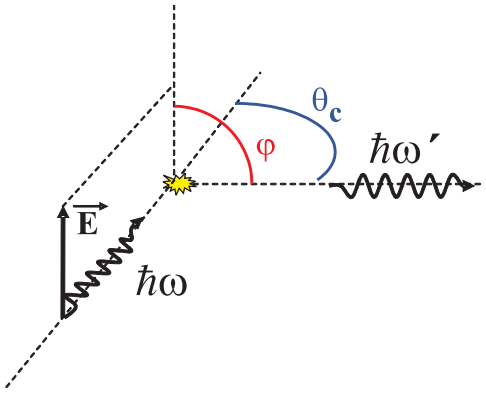

Figure 4.10: Definition of Compton scattering angle θ and the azimuthal scattering angle ϕ relative to the polarization vector $\overline{E}$.

The differential cross section for Compton scattering into a solid angle element $d\Omega$ is given by the Klein-Nishina formula:

$$\frac{d\sigma}{d\Omega} = \frac{r_0^2}{2}\frac{E_\gamma'^2}{E_\gamma^2}\left(\frac{E_\gamma'}{E_\gamma} + \frac{E_\gamma}{E_\gamma'} - 2\sin^2\theta\cos^2\phi\right) \tag{4.2}$$

where $r_0 = \frac{e^2}{4\pi\epsilon_0 m_e c^2}$ is the classical electron radius. The scattering cross section is enhanced in the direction perpendicular to the polarization vector of the incoming photons, as visualized in fig. 4.11.

The sensitivity of Compton scattering to the polarization of photons of a given energy is expressed as the quantity known as the *modulation fraction* [56]

$$M(\phi) = \frac{N(\phi + 90°) - N(\phi)}{N(\phi + 90°) + N(\phi)} \tag{4.3}$$

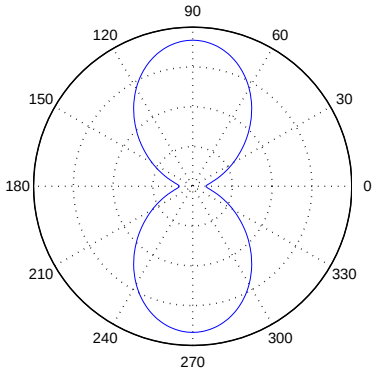

Figure 4.11: Azimuthal dependence of the Compton scattering cross section relative to the polarization vector of the incoming photons. The photon energy is 288 keV.

where $N(\phi)$ is the intensity of scattered photons into the angle ϕ. The maximum of $M(\phi)$ is reached when $N(\phi + 90°)$ is at its maximum and $N(\phi)$ is at its minimum. From fig. 4.11, it is evident that this occurs at $\phi = 0$. Figure 4.12 shows the variation of the modulation fraction as a function of the scattering angle θ. We see that the polarization sensitivity decreases with the photon energy. The maximum of $M(\phi)$ is at $\theta = 90°$ in the low-energy limit. With increasing energy it shifts towards somewhat smaller angles. This feature can be utilized in the construction of a polarimeter – a detector system favouring slightly forward-scattered events has an advantage for higher energies.

Rayleigh scattering can also be used for polarimetry as described later in this chapter. These methods were later successfully used in the measurement of polarization properties of electron bremsstrahlung performed at the polarized electron injector of S-DALINAC at TU-Darmstadt.

4.6.1 Summary of paper II: Compton polarimetry with the planar detector

In order to test the performance of the 25-pixel detector as a polarimeter, a measurement using a ^{137}Cs source was performed. The 661.7 keV γ-rays were collimated towards a non-segmented coaxial HPGe detector. The Compton-scattered radiation from this detector is the source of linearly polarized photons that were analysed by the 25-pixel detector. 661.7 keV photons scattered at 90° result in polarized 288.3 keV photons and a 373.4 keV energy deposit in the scatterer. Due to the large size of the detectors, the possible scattering angles for events with a single interaction in the coaxial detector vary from 85.5° to 95.0° resulting in energies measured in the coaxial detector between 360.0 keV and 386.8 keV.

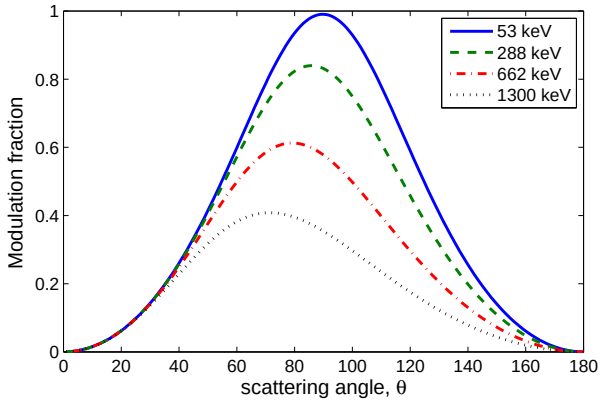

Figure 4.12: The dependence of the modulation fraction on the scattering angle for some energies.

Data was collected for all events where the two detectors triggered in coincidence. Those events where exactly two of the segments of the planar detector had triggered, with the total energy of 288 keV, were used for the polarization measurement. In the off-line analysis, a narrow energy gate was applied to the total energy deposit in both detectors. A further energy gate is then set for the energy in either one of the detectors. This ensures that the photons scattered once at angles close to 90° in the coaxial detector are selected.

Analysis was performed both with and without the use of PSA. For the analysis without the use of PSA, the events were analysed separately depending on the distance between the two segments. In the measurement with the 288-keV photons, in approximately 90% of the events, photons scatter between two adjacent segments, 9% scatter across 1 segment and 1% across 2 segments (very few scatter across 3 segments). This is due to both the increased absorption in the detector material between distant segments, as well as the lower number of segment combinations contributing to a given scattering direction.

Without PSA, a number of scattering directions are defined by vectors connecting the centres of the pixels, with the majority of directions represented by several segment combinations. When PSA is used to reconstruct the interaction points, it becomes possible to perform kinematic event selection, i.e. selection based on θ. The position resolution obtained in the imaging measurement (section 4.5) constraints the scattering angle, θ to a range of values. This range depends heavily on the separation of the interaction points. While the average position resolution for a pair of interactions in neighbouring segments is 1.5 mm, as shown in section 4.5.1, the resolution is likely to deteriorate when the interactions are very close to each other (on the respective sides of the segmentation boundary). Therefore, in or-

der to reject pairs of points closer than twice the position uncertainty, for which no constraint can be put on θ, a minimum distance of 5 mm was set for events used. Furthermore, the Compton scattering formula was used to test whether the obtained range of angles θ is consistent with the energies measured in the two triggered segments. Events that do not fulfill this condition are likely to consist of more than two interaction points and were rejected. Finally, angles θ lying between 56° and 116° were selected in order to maximize the polarization sensitivity, see fig. 4.12.

The scattered intensities measured for different directions will vary greatly due to the geometries of the two segments involved as well as the distance between these segments. Assuming that the detector is symmetric under a 90° rotation, one finds that such geometrical effects for a scattering direction ϕ are identical to those at the angle $\phi + 90°$. Therefore scattered intensities, $I(\phi)$ were normalized using [57]:

$$I_{norm}(\phi) = \frac{I(\phi)}{I(\phi + 90°)} \tag{4.4}$$

for scattering directions obtained using both the centers of the pixels as well as for the PSA-reconstructed points. For the normalized intensities, the dependence on geometrical factors is removed.

A modulation fraction of 0.485 is expected for 288 keV γ-rays that are produced through Compton scattering of 662 keV primary γ-rays for the relevant range of scattering angles defined by the geometry of the experiment. Both methods tend towards this value. When only pixel resolution is used, however, this sensitivity is only achieved for well-separated segments, i.e. only at a low efficiency. The use of PSA makes it possible to obtain significantly higher polarization sensitivity for the cases of close-lying segments. The results are shown in table 4.1. Modulation fractions have been determined for all events as well as separately for each inter-segment distance.

Segment separation	N_{events}	M_{max}(pixel)	M_{max}(PSA)	PSA selection
all	85733	0.173	0.350	∼20%
0	76928	0.156	0.345	∼12%
1	7650	0.306	0.351	∼100%
2	1155	0.417	0.427	∼100%

Table 4.1: The measured modulation fractions and the number of events contributing to each segment separation. The approximate percentage of events left after kinematic event selection following PSA reconstruction is shown in the right-most column.

Using PSA-reconstructed interaction locations, allows the selection of events with the greatest sensitivity to polarization even in cases of close-lying interactions, as well as to reduce the number of events with multiple scattering points. Approximately 20% of the events were kept in this case – the majority of the

events separated by at least one segment as well as approximately one in eight of the adjacent-segment events. This possibility is important for low-energy γ-rays in particular. When the mean free path of the photons becomes too short to obtain a significant number of events with separated segments, a high polarization sensitivity can none the less be obtained using the adjacent segments and applying PSA.

4.6.2 Rayleigh polarimetry

Effects of linear polarization of photons can also be observed by measuring the angular distribution of Rayleigh scattered photons. This technique was experimentally evaluated for the first time using the KTH pixel detector, and is descried in paper 5. A beam of 53.5 keV photons was produced by 59.5 keV photons from a ^{241}Am source Compton scattered at 90° off an aluminium target. The resulting photons are nearly 100% polarised (see fig 4.12). A narrow beam was selected using a lead collimator. At the exit point of the collimator, a lead foil was placed where Rayleigh scattering could occur. The pixel detector was placed directly down stream of this beam. A thicker lead absorber prevented the detection of unscattered photons that would otherwise hit the central segments of the detector or the detector housing (where further scattering may otherwise occur). The outer 16 segments were then used to measure the angular disctribution of the scattered photons.

The Rayleigh scattering cross section exceeds the Compton cross section at low photon energies. On the other hand, the cross section for photo absorption is always greater than for Rayleigh scattering (see for ex. fig. 1.1). Therefore the efficiency of this type of polarimetry is significantly lower than for Compton polarimetry, assuming that the comparison is made at the energies where each method is preferred. Due to a negligible scattering energy deposit as well as the strong forward-focusing of Rayleigh scattered photons, it is not practical to use an active scatterer, as described in section 4.6.1 when relying on Compton effect. While this prevents the use of coincidence technique, it also allows for a much more well-defined scatterer location and a free choice of the scatterer material (high atomic number is preferred here).

A large advantage of Rayleigh scattering for the polarimetry application is that the scattered photons are practically monoenergetic, resulting in a well-defined peak. This makes rejection of background and unwanted Compton scattering components (such as scattering in the collimator walls or other parts of the set-up) significantly easier. Nevertheless, in an experiment such as described here, care must be taken when choosing the geometry of the set-up and the materials used, since photons Compton scattered at small angles loose only a small portion of their energy. These may be difficult to distinguish from Rayleigh scattered photons due to a finite detector resolution.

Chapter 5

DESPEC tracking detectors

This chapter presents the applications of PSA and γ-ray tracking in the germanium arrays for nuclear structure studies proposed for the new FAIR facility. Sections 5.1 and 5.2 present general goals of the research and the advantages of position-sensitive germanium detectors in this facility. Sections 5.3, 5.4 and 5.5 present the contribution of this work to the development of the DESPEC array. All analysis in this chapter is based on simulated data.

5.1 Research at FAIR

The international accelerator facility FAIR – Facility for Antiproton and Ion Research – will be built at the site of the existing GSI facility near Darmstadt, Germany. The current GSI facility provides primary beams of highly charged ions of in principle any stable elements from $^{1}_{1}$H to $^{238}_{92}$U. Short-lived radioactive beams can be produced by fragmentation or fission of the ions in these beams. Desired isotopes can then be isolated in the Fragment Recoil Separator (FRS) and transported to secondary reaction targets or deposited in storage rings. Furthermore, beams of ^{12}C are used for radiation therapy.

At the new facility the primary beam intensities of up to 10^{12} ions/s (100-1000 times more than the present facility) and energies of up to 1.5 GeV/A will be reached with the SIS 100/300 synchrotron. The new Super-conducting Fragment Recoil Separator (SuperFRS) will provide higher selectivity, transmission and energies of secondary beams [58]. Several larger synchrotron rings will be built for accelerating and storing the wide range of ions currently available with the addition of antiprotons.

NUSTAR (NUclear STructure, Astrophysics and Reactions) is one of the biggest research programs at FAIR. Research will be based on exotic beams delivered by the SuperFRS to various experimental areas, where, in many cases, germanium detectors will be used. The low-energy branch will house experiments where collisions of radioactive secondary beams with stationary targets produce nuclei further

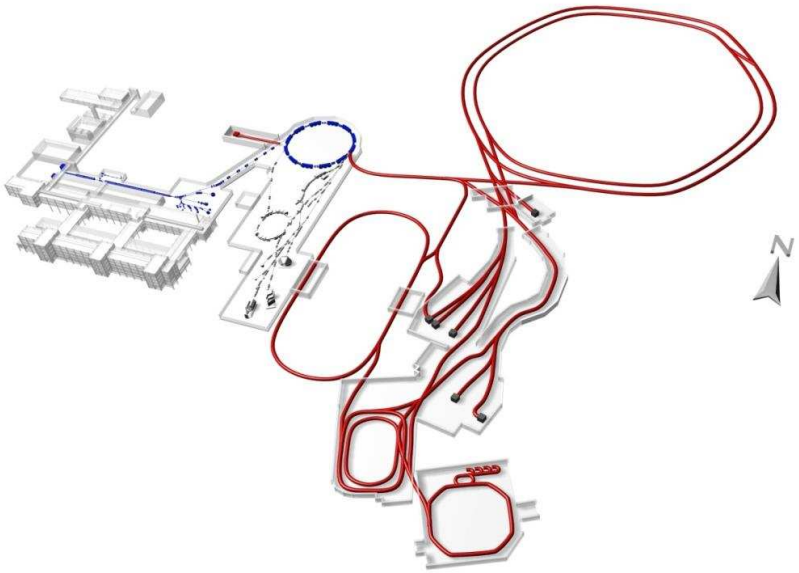

Figure 5.1: The schematic of the existing GSI facility (the part on the left) and FAIR (on the right). New beam lines are shown in red.

from stability than has previously been possible using stable beams. Properties of these nuclei will be analysed using various combinations of the following detector systems: HISPEC (High-resolution In-flight SPECtroscopy), DESPEC (DEcay SPECtroscopy) and LASPEC (LAser SPECtroscopy), MATS (ion traps). The R^3B (Reactions with Relativistic Radioactive Beams) set-up is designed for nuclear reactions at much higher energies. Finally, storage rings will be built that will allow to contain fully or nearly fully stripped ions. Here, eg. physics specific to decays of bare nuclei can be accessed. These conditions can be compared to nuclei in environments relevant to astrophysics. Furthermore, histories of individual ions as they are revolving in a storage ring can be traced.

The PANDA detector set-up is aimed at various hadron physics studies involving collisions of antiprotons with nuclei [59]. A germanium array is envisaged as a part of this experiment for high-resolution γ-ray spectroscopy of hypernyclei (i.e. nuclei in which some of the nucleons contain strange quarks) produced using antiproton annihilation at 3 GeV. PSA and γ-ray tracking techniques may also be applied in this array in order to perform background rejection as well as discrimination between particles and γ-rays. Since for the purposes of particle identification,

strong magnetic fields will be used, the performance and pulse shape formation in germanium detectors will be significantly modified.

5.1.1 DESPEC: decay spectroscopy

In many experiments, one needs to detect γ-rays and other decay particles emitted that are delayed by of the order of μs to ms with respect to the production time of the nucleus under study. There are two main classes of experiments where this is important – decay tagging and decay spectroscopy of isomeric states.

Decay tagging is a powerful technique in in-beam spectroscopy where the isotope produced in each individual collision is identified through the detection of its characteristic decay. It can be implemented in experiments where both HISPEC and DESPEC arrays are used. Prompt photons from a produced nucleus are detected in a detector array surrounding the reaction target. The nucleus, however, is not stopped here but transported through a magnetic spectrometer to an active stopper, such as a thin silicon double sided strip detector (DSSD). Here the positions of the implantations and the subsequent decays (for example α- or β-decays) are determined. By correlating these with the events at the target, extremely rare isotopes can be selected, provided that a suitable decay mode exists[1]. This technique is extensively employed in the JUROGAM/RITU/GREAT set-up in University of Jyväskylä, Finland. One of the many successful experiments is described by Sandzelius et al. [60].

A decay spectrometer is also essential in cases where an exotic nucleus has a meta-stable state. A γ decay of a state with a life time of more than a few ns cannot be detected at the target position if the recoils are not stopped. By implanting the recoil in an active stopper, photon emissions from a decaying meta-stable state can be correlated with the implantation position and the prompt photon/particle emission. A requirement for such correlation is either a characteristic decay following the decay of the isomeric state, or, as also proposed for the DESPEC array, the ability to use γ-ray tracking and imaging techniques in order to correlate the photons with an implantation position. This type of experiment is the continuation of the concept successfully used in the RISING stopped beam campaign [61] at GSI and experiments such as described in ref. [62].

Some of the detector systems included in the DESPEC proposal [14] are:

Silicon implantation detector AIDA (Advanced Implantation Detector Array) will be used as the active stopper. It consists of several thin 8×8 cm silicon DSSDs that can be arranged in 8×8 or 8×24 cm configurations. These detectors must have a very wide dynamic range in order to detect energy deposits as low as 100s of keV from β decays and a few MeV from proton or α decays to tens of GeV from the stopping of heavy ions. Another challenge is the

[1] Isotope production cross sections of the order of 10 nb have been reached – a record in γ-ray spectroscopy.

requirement of sub-ns timing, since time-of-flight information will be used in particular for neutron spectroscopy.

Germanium array used for high resolution decay γ-ray spectroscopy is described in detail in the following sections.

Neutron detectors will be used to study ground state or β-delayed neutron decay of neutron-rich nuclei either in combination with the Ge array or instead of it. Two types of neutron detectors are being developed: a time-of-flight spectrometer based on liquid scintillator detectors and a 4π detector with ^{3}He active elements.

Total absorption spectrometer is a scintillator-based photon detector optimized for maximum efficiency and solid angle coverage.

LYCCA (Lund York Cologne CAlorimeter) is an array of fast position-sensitive silicon (alternatively diamond) detectors and CsI calorimeters, that will identify fast ions (100-200 MeV/u) using time-of-flight and E/ΔE measurement.

The HISPEC systems' development is closely related to DESPEC. Where DESPEC instruments are optimised for measurements with stopped nuclei, HISPEC is the system that will be used at the target position to measure emissions from fast nuclei and resembles the set-up for the fast beam campaign at RISING [61]. Many combinations of instruments of HISPEC/DESPEC are envisaged for various experiments.

5.2 Advantages of γ-ray tracking

Both HISPEC and DESPEC high resolution γ-ray spectrometers will consist of germanium tracking arrays. In HISPEC, the photons of interest originate in (or near) the reaction target, and in DESPEC in the silicon wafers of the implantation detector. Various sources of background photons exist:

Prompt flash: The ions stopping in the silicon detector emit bremsstrahlung photons as they slow down and x-rays from recombination of the ion with electrons.

Beam line: In many cases, ions will pass through various materials before arriving at the implantation detector – beam degraders, or beam particle detectors – emitting similar radiation to the case above.

Activation: Nuclear reactions with materials other than the intended target as well as the decaying isotopes starting from the implanted ions generate background γ-rays.

Environment: Photons from decays of naturally occurring radioactive isotopes and cosmic rays contribute to a relatively isotropic background.

In the proposed DESPEC array, tracking and imaging techniques should allow the reconstruction of the origin of a photon to a cone of possible directions. It is then possible to verify whether a photon may have originated from the implantation detector (and with a high-enough spatial resolution, whether or not it may have originated from a particular pixel where a decay took place) or from a direction of a beam detector or another source of background. Furthermore, timing may be used to make such discrimination – a photon coincident with an implantation signal is likely to be from the prompt flash or from the passage of beam detectors and can be removed, while those correlated with α- or β- or other types of decays should be used. In cases where no correlation can be found, the photon likely comes from activation or natural background.

The goals of tracking in HISPEC are somewhat different. This array, needs to handle much larger γ-ray multiplicity from prompt decays of excited states. Therefore an ability disentangle close-lying interactions of two or more γ-rays is important. Furthermore, since HISPEC will typically be used with fast beams, a large gain in energy resolution can be achieved by Doppler correction. γ-ray tracking provides a much greater accuracy in the determination of the emission angle of photons with respect to the beam direction as compared to conventional array, where the detection location can only be determined with the precision of the size of the crystal (or segment).

Applying tracking to reconstructed interaction locations can also allow a degree of Compton background rejection [63]. This can be achieved by calculating a figure of merit for a possible track with and without the assumption that the track is a full absorption event. With an appropriate choice of the figure of merit it is then possible to make a decision to keep or reject the event.

The performance of the germanium detectors, in particular their spatial resolution, will determine the possible level and complexity of the data analysis described above. Monte Carlo simulations are required in order to evaluate the performance in various configurations and under different experimental conditions. Generally, such studies involve several steps.

Event generator: A realistic γ-ray flux should be generated including the origin of the photons, the time of emission and energy. Measured data from an experiment using previous generation detector set-ups can also be used.

Interaction simulation: The generated photons must be transported through the detector system and their interactions simulated. This step results in positions and energies of interactions in the detector volumes.

Pulse shape analysis: The detector signals corresponding to the simulated interaction positions and energies are calculated. With the addition of relevant noise contributions, these are treated as experimental signals. From this point on, the analysis mirrors the data processing that is to occur in a real experiment. The pulse shapes are analysed in order to reconstruct the associated interaction positions and energy deposits.

Tracking: The interaction locations reconstructed by PSA are assigned to tracks traversed by photons, and, if necessary, the origin of a photon is estimated. Decisions are then taken as to whether the photons are kept or not.

Papers 3 and 4 focus mainly on the PSA step in the analysis above for the three detector types – pixel, strip and clovers. In this work, several fixed energies were used originating from the implantation detector (*source events*) or isotropically anywhere else (*background events*). Each array was simulated in GEANT4 [64]. In this case, only the germanium volume was simulated and the inactive elements such as the cryostats, detector supports and electronics were neglected. The main result of the work published in papers 3 and 4 is the attainable position resolution as a function of photon energy and complexity of the event for three detector types. The results of tracking are presented in paper 6 focusing on the attainable improvement in the final spectra, in particular the peak-to-total (P/T) ratio and the background suppression factor.

5.3 DESPEC Ge array

A number of different detector types and configurations have been considered for the germanium array. One of the proposed configurations consists of 24 detector modules, each housing three planar crystals in a single cryostat. The arrangement of the three crystals is shown in fig. 5.2. The size of the crystals is 72×72×20 mm. The triple modules are then placed in a box configuration around AIDA as shown in fig 5.4.

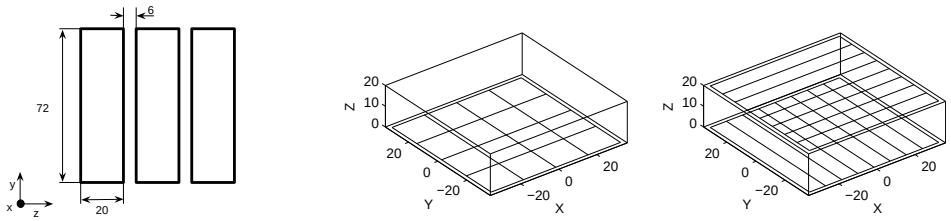

Figure 5.2: The triple planar module and pixel and strip crystal segmentations considered in this work. The dimensions are given in mm.

Two types of planar segmented detectors are considered for this configuration – a pixel detector, similar to the detector described in section 4.5, and a double-sided orthogonal strip detector. In this work a comparison has been carried out for a 4×4 pixel detector with 17×17 mm pixels and an 8-by-8 strip segmentation with a strip pitch of 8.5 mm. This choice is made in order to have the same number of readout

channels. In both cases, 2-mm wide guard rings are assumed. The geometries are illustrated in figure 5.2.

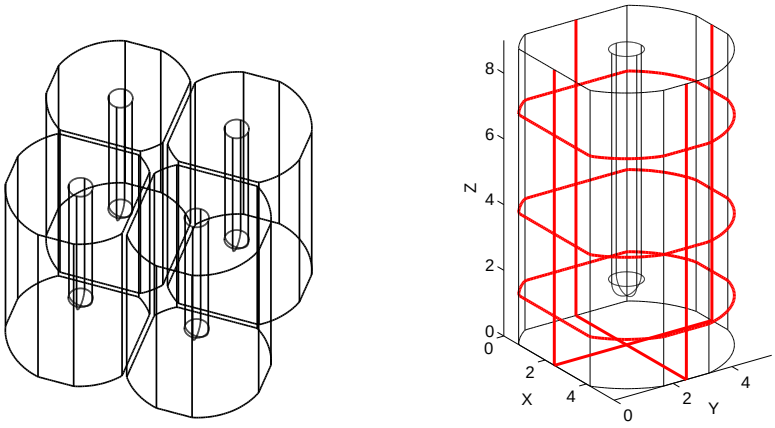

Figure 5.3: The clover 4-crystal module and an example of a segmented crystal. Segmentation lines are shown in red.

Another alternative considered was segmented clover detectors similar to the TIGRESS and EXOGAM detectors but with a higher degree of segmentation. Such a detector is schematically shown in fig 5.3. In addition to the increased segmentation these detectors were not tapered in the simulation in the same way as the existing clovers since they would be placed around a rectangular implantation detector rather than a spherical target chamber[2]. Six clover modules result in approximately the same total volume of germanium as the planar array. The array of 6 clovers is shown in fig. 5.4.

A note on nomenclature

The crossing strips define a larger number of voxels than possible with the same number of pixels. In order to avoid confusion let us define the **segment** – namely the volume which contributes to the signal on a given contact; and **voxel** – the smallest volume element defined by simple readout (without PSA). The reason this distinction is convenient is that a segment is a unit of the electronic readout – something that yields a pulse shape, an energy and a timing measurement. The voxel is the unit of physical spatial resolution of the detector if no PSA is applied. In detectors with only one segmented contact, such as pixel and clover detectors, segments are identical to voxels. When it comes

[2]Realistically, the front edges would likely be rounded in order to remove low-field regions and achieve full depletion. This was neglected in the simulation.

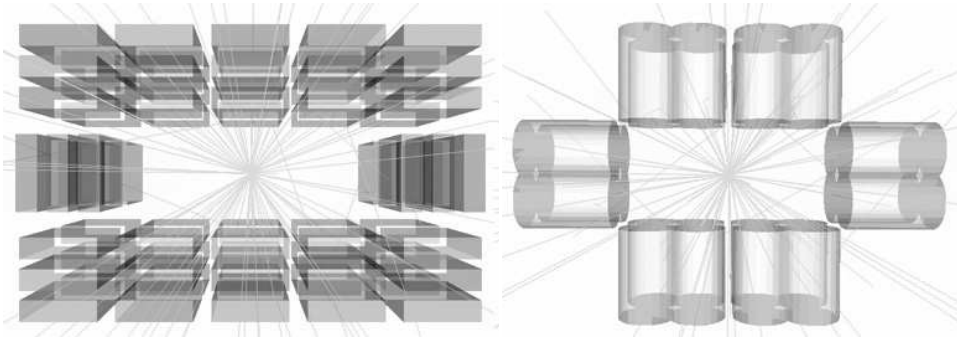

Figure 5.4: **Left:** planar detector crystal arrangement for the full array of 24 triple modules. **Right:** clover detector crystal arrangement for the full array of 6 clover modules.

to the strip detector however, the voxels are formed by the intersections of the segments.

5.3.1 Clover detector segmentations

A number of different segmentations along the depth of the detector have been considered. These are summarised in table 5.1. Notation of the form $a-b-c(-d)$ is used here, referring to a detector where the first lateral segmentation line is a mm from the from the front face of the crystal, the second is b mm further and so on. Additionally, a test has been made with the longitudinal segmentation rotated by 45° with respect to the standard segmentations (in the case of the 15–25–25–25 segmentation). In this configuration, the longitudinal segmentation lines run along the curved sides of the cylinder rather than the flat sides. In all cases the main crystal axes, <100>, are oriented along x-, y- and z-axes (see fig. 5.3), i.e. perpendicular to the flat surfaces.

There are a number of concerns when selecting a segmentation pattern for a coaxial crystal. The detector is irradiated from the front and therefore a larger fraction of events is expected in the front part. On the other hand this is not true for background photons from various sources. The segment rings in the middle of a crystal were found to have the best position resolution – not surprisingly, since these segments have a neighbour on each of the four sides. The front and back segments have only three neighbours. With similar depths of the segments throughout the detector, a clear degradation of the resolution is seen in these. In the case of the back segments, the biggest error component originates from the depth coordinate – especially for events that are far away from the front of these segments, where the depth coordinate is only given by the very weak transient signal from the segment in front of it. The segments in the front ring also show lower resolution, however

in this case, in all three coordinates.

number of segments	depth segmentation, mm	mean error for 1-interaction events, mm
12	25–25–40	3.43
12	20–40–30	2.71
16	20–25–25–20	2.08
16	15–25–30–20	2.09
16	15–25–25–25	2.19
16 (45°)	15–25–25–25	2.05

Table 5.1: Segmentations of clover detectors tested in this work and corresponding mean position errors. The notation shows the distances from the front of the detector to the first segmentation line, from the first to the second, and so on. Mean errors are given for single-site 662 keV interactions.

In order select one of the clover segmentations for comparison with the planar arrays a test of average position resolution and its uniformity from segment to segment was performed. A set of 16000 simulated randomly distributed single interactions of 662 keV were reconstructed for each segmentation. Position reconstruction error was defined as the distance from the original point to the reconstructed one. Table 5.1 shows the average resulting position error across all segments[3]. The segment numbering scheme is shown in fig. 5.5. A segment-by-segment position error comparison for each Cartesian co-ordinate is shown in fig. 5.6 for all clover crystals considered. Note that there is a large variation between the rings of segments, for instance the largest contribution to the mean error for the 25–25–40 detector is from the depth coordinate in the back segment (∼6 mm) and from all coordinates in the front segments to a somewhat lower degree. Furthermore there is a slight but apparently systematic variation between the segments within a ring. The small segments (4, 8, 12, 16) and the big segments (2, 6, 10, 14) show a smaller error than the medium-size segments (all other segment numbers). It was found that reconstructed positions in the middle rings shift primarily in the azimuthal direction to form a cluster near the centre of the segment (see fig. 4.1). This effect appears to be stronger in the medium segments and increases with noise level.

The segmentation 15–25–30–20 was chosen for the analysis in paper 4 due to the most uniform position resolution throughout the detector. Here the front and back segment rings are made shorter for a better position resolution. The third ring was made somewhat deeper than the second since the electric field is the most regular in this part and this seems to improve the reconstruction accuracy. Furthermore the third ring is further away from the implantation site and is less likely to contain multiple interactions. The rotation of the segmentation by 45°

[3]Rather high energy single interactions have been considered here, and so these position errors are not directly comparable to those presented in section 5.4 and papers 3 and 4, since there averages for more realistically distributed energies are used.

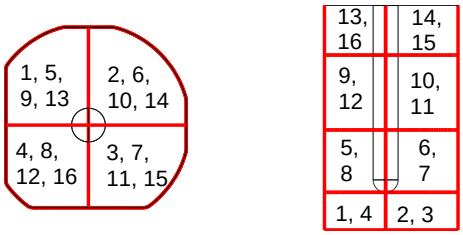

Figure 5.5: Segment numbering for a clover crystal.

was found to slightly improve the resolution[4]. However, since to date, no clover detectors have been manufactured in this way, it was not kept as the final choice.

A note on the definition of position resolution
In various works where position sensitive detectors are characterised, different definitions of position resolutions are used. Generally, the term *resolution* implies the minimum separation of two positions, energies, or other types of parameters for which a clear discrimination could be made. This is often well described by a width of a peak at half its maximum height (FWHM). This type of definition was judged to be inappropriate in the present analysis for the following reason. The simulated interactions are distributed continuously throughout the detector volume, as are the reconstructed locations. The FWHM applies when a value needs to be placed in either one discrete group or another (as for example for two closely-lying lines in an energy spectrum). This is never the case with the position reconstruction as used here. This reasoning holds also for reconstruction using algorithms that select only one basis point in the reconstruction procedure, since the real interactions are spread continuously and are only assigned to a discrete location as an approximation. The use of FWHM for position reconstruction may be justified, however, when analysing scanning data, since in this case the goal may be to distinguish between discrete collimator positions. Although the real interaction position is never known with more than a few mm accuracy, which is often more than the inter-point distance in a basis grid.

A note on the term *position sensitivity*
In some studies a position sensitivity presented is well under 1 mm,

[4]It may be interesting to note that in the TIGRESS detectors, the *crystallographic axes orientation* is turned by 45° (i.e. the <100> axes lie along the z-axis, and $y = -x$ and $y = x$ lines), while the segmentation is made in the conventional way.

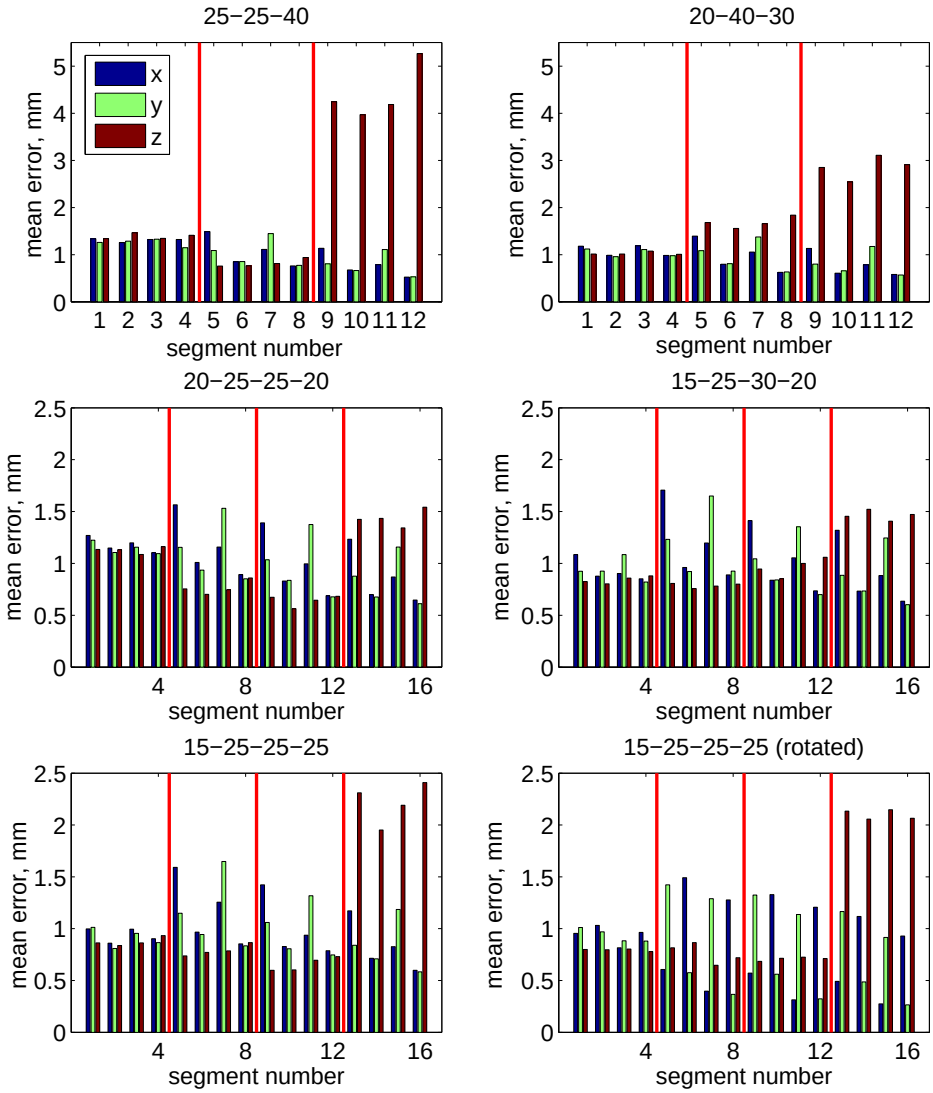

Figure 5.6: Position errors for the 6 clover segmentations considered. Mean errors are shown for each segment and co-ordinate. The vertical lines separate the groups of 4 segments in the same ring.

whereas recent experimental results indicate that realistically obtainable position resolution is on the order of 4-5 mm in detectors such as AGATA [15, 65]. It is important to make the distinction that in many cases, *position sensitivity* rather than *position resolution* or *position error* was determined. Position sensitivity can be obtained, for instance, by varying the position of a simulated interaction or of a collimator in a scan until the resulting difference in the pulse form with the inclusion of noise is statistically significantly different from the previous one. Such a quantity does not necessarily represent the accuracy of the position of a reconstructed interaction. In particular, various interaction locations from well-separated parts of a detector, or combinations thereof, can result in indistinguishable pulse shapes. Such and similar effects are naturally included when reconstructing positions from pulse shapes, but are completely ignored in the procedure described above. In this work, position resolution is given for reconstructed events in all cases.

5.4 Summary of papers III and IV: PSA simulation

Photons with energies of 200, 600, 1200 and 2000 keV were simulated for the analysis with planar detectors in paper 3. For the comparison in paper 4, photons of 250, 662 and 1332 keV were used with all three types of proposed detectors for DESPEC. The interaction points within the array of germanium crystals were simulated in GEANT4. The resulting pulse shapes for each detector crystal and segment were determined for the pixel, strip and the 15–25–30–20 clover detectors as described in section 2.6. These were stored and, with added noise with the maximum amplitude corresponding to a 2.5 keV signal, treated as experimental data. Energies in each segment were determined as the sum of energies of all interaction points in the the segment volume.

The simulated pulses were analysed using the matrix method described in section 3.3. The total number of segments is 16 for the strip detector, 17 (including the non-segmented one) for the pixel detector and 13 or 17 for the clover crystals. The sampling frequency was reduced to 50 MHz. For the planar detectors 12 pulse samples per segment were used. In case of clover detectors, charge collection times can be somewhat longer than for the planars, therefore 20 samples were used. The matrices described in section 3.3 were prepared for single and double voxel interactions.

The segments far from the interaction points were not discarded, resulting in meta-signals of a constant length. The data reduction would not be significant in the case of the detectors in question. The events that truly bottleneck the calculation are the ones with more than two voxels triggered, for which there are no pre-calculated matrices. For these, the number of necessary segments (ones with net charges and their neighbours) can often be close to the total number of segments. Therefore it was judged that a segment selection would impair the algorithm more

than benefit it.

All interaction points in a voxel returned by the matrix algorithm were merged and replaced by a single centre-of-energy point. On average, for a complete detector module, 18% of the events in the strip detectors and 30% in the pixel detectors, 40% in the 16-segment clovers and 50% in the 12-segment clovers had some merged points in at least one of the detector crystals due to this effect.

A number of different basis grids using different densities of basis points were tested with the planar geometries. The number of basis points defines the size of the matrices used in the matrix method (n in eq. 3.3–3.8), and must therefore be optimized to make the CPU times manageable. It was found that relatively sparse grids performed adequately. For clover detectors, only one grid for each of the 6 segmentations was used. This grid was dimensioned so that the density of the basis points at the outer radius of the detector is on the order of that of the planar detectors with the sparse grids. The density close to the core is much higher. This is in principle unnecessary, however, for simplicity, the number of basis points in the 3 coordinates (r, ϕ, θ) was kept constant. The basis point positions in the vicinity of the depth segmentation boundary were adjusted so that the layers of basis points curve along the boundary on each side. A segmentation boundary is shown in fig. 5.7.

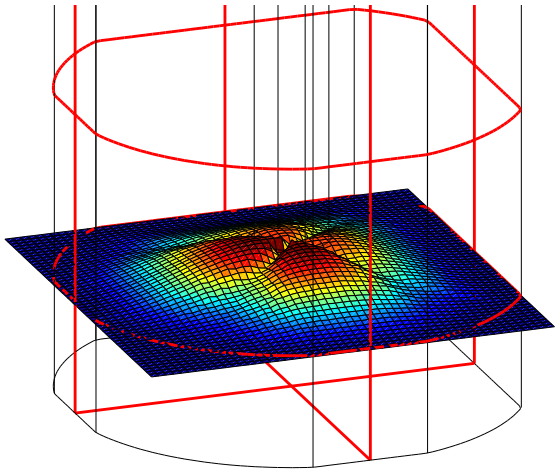

Figure 5.7: The boundary between the first and second ring of segments in the 15–25–30–20 clover. The maximum hight of the surface is approximately 20 mm (5 mm above the segmentation line).

5.4.1 Summary of detector comparisons

Table 5.2 summarises the mean position errors obtained for the strip and pixel planar and for the 15–25–30–20 clover detectors. Average errors for interactions of all energies occurring in the data set are shown. Overall, the position errors scale with the physical segmentation size, resulting in a significant advantage for the strip detector. This is in addition to the lower likelihood of merging of interaction points in this detector. On the other hand, the disadvantages of the strip planar detector include the much larger number of voxels and therefore a larger amount of pulse shape basis data stored in the computer memory. Furthermore, some combinations of voxels hit in the same strip crystal cannot be uniquely identified. These disadvantages become more significant for the case of high γ-ray multiplicity, a situation that can arise when the prompt flash arrives simultaneously with the nuclear decay. Such complications would be avoided entirely in a pixellated detector with a physical granularity equal to that of the strip detector discussed here. This would, however, require a much larger number of readout channels (64 for identical granularity). Further discussion can be found in paper 3.

Detector	planar	planar	clover
	16-strip	16-pixel	15–25–30–20
basis grid	5×5×14	7×7×14	64×14×44
single total	1.14	2.13	3.41
multiple total	2.20	3.92	6.63
single, merged	2.11	3.23	4.48
multiple, merged	2.58	4.24	7.39
single, non-merged	0.99	1.79	2.85
multiple, non-merged	2.05	3.68	6.04

Table 5.2: Comparison of the strip, pixel and clover detectors. Mean errors in reconstructed positions are given in mm and are presented for single and multiple-voxel interactions. Average errors for all events are given in the first two rows and those for merged and non-merged interactions separately in the following rows. The values are averages over all energies.

The position error is defined as the mean Cartesian distance of the reconstructed position relative to the interaction positions simulated in GEANT4 as in section 5.3.1. Events with multiple interactions per segment were included in all cases. Since only one location is reconstructed per segment, the position error for these events was defined as the distance from the centre of mass of the simulated interactions to the unified reconstructed location.

5.4.2 Energy dependence of position error

In many events photons Compton scatter more than once before full absorption. Therefore a continuous range of energies is available among the reconstructed data.

Fig. 5.8 shows the mean position resolution as a function of energy for each detector type. This result is presented separately for single-segment and multiple-segment interactions. The distributions of errors around the mean are not symmetric. This is indicated by bars in the fugures, whose lengths correspond to standard deviations calculated separately for error less and greater than average.

This result can be useful when dimensioning detectors for applications with specific photon energies such as in various imaging applications. The position resolution dependence on energy for single-segment events can be attributed to the increasing relative amplitude of electronic noise with decreasing interaction energy. A further effect is that there is likely to be more merged interactions among high energy events. It has not, however, been evaluated in detail whether and how this contributes to a the average position error. For multiple-segment interactions, position resolution is generally worse, as expected. Since in situations with several interactions, the position of the lower-energy one tends to be more difficult to reconstruct, the position resolution degrades faster for lower energies than in the case of the single-segment events.

5.4.3 Tracking

The PSA-reconstructed data was used as the input to a tracking algorithm designed for DESPEC detectors [63]. These results are presented in paper 6, where also the performance of a reduced planar array composed of 16 triple modules is considered. The two main parameters considered are the background suppression factor and peak-to-total (P/T) – in other words the efficiency of rejection of stray photons and Compton continuum events. The values of these parameters can be improved to some extent at the expense of the total tracking efficiency if the limits on the relevant figures-of-merit are tightened.

The pixel detectors were found to have approximately 10% lower tracking efficiency if the same P/T performance is demanded. Comparing the planar array based on strip detectors to the clover array, a large advantage of planar detectors is seen. The highest tracking efficiency obtainable in the clover array is only comparable to the planar array for the highest energy (1332 keV) and is approximately a factor 2 worse for the lowest energy considered (250 keV). Background supression and P/T are worse for the clover array for a given efficiency in most situations.

5.5 Outlook: Realistic experiment simulation

In the analysis above, a rather simplistic assumption of photon energies has been used. While allowing a position reconstruction evaluation for a set of representative energies and irradiation directions, such analysis does not fully represent the performance of the array in a real experiment. Before a decision on the configuration of the Ge array can be made, it's performance needs to be compared to conventional arrays such as that used in RISING. It is not likely that any of the proposed tracking arrays will show a better raw germanium efficiency than that obtained

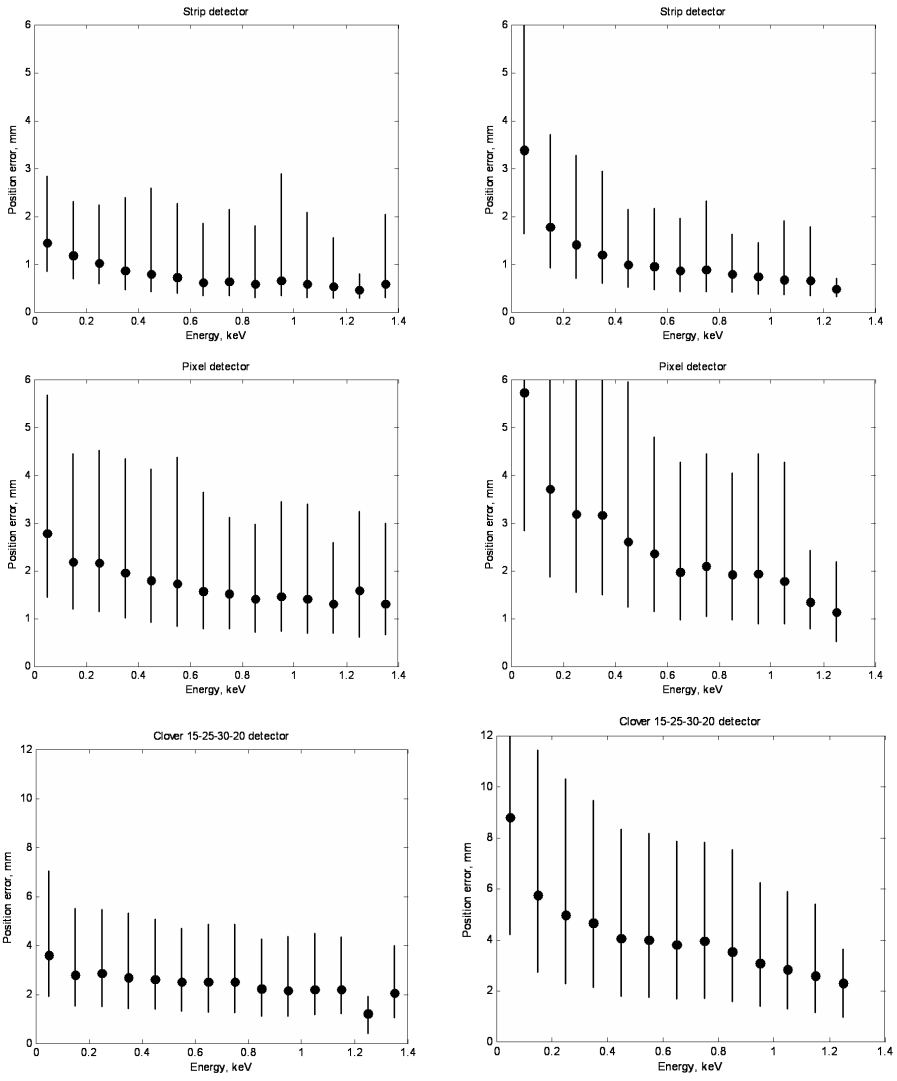

Figure 5.8: Position resolution for the tree detector types and as a function of γ-ray energy. **Left:** single-segment interactions, **right:** multiple-segment interactions. Note that the vertical scale is doubled for clover detectors.

with RISING (∼10%) – the Cluster detectors already have a large depth (9 cm) and a large solid angle coverage. The latter cannot be increased by much since in a majority of experiments part of the solid angle will have to be occupied by other types of detectors (eg. neutron) as well as electronics that in some cases (as with AIDA) must be placed very close to its detectors. The gain of the tracking array lies instead in its selectivity, background rejection and in the possiblility to distinguish between the decays of many implanted nuclei simultaneously. These features should allow operation at higher rate and increased sensitivity to longer isomeric or decay lifetimes. There are several aspects that may need to be addressed in details before a realistic gain can be determined.

A full simulation should include tracking of the ions through any relevant materials in the vicinity of the detectors and their stopping in the implantation detector. At each of these locations, bremsstrahlung and x-rays may be emitted. The relevant spectra have been characterized for RISING experiments [66]. The decaying isotopes then emit characteristic γ-rays at some later time. Generally, the multiplicity expected is not as high as in the case of a detector placed at a reaction target position, as in the case of HISPEC. A typical γ-ray multiplicity on the order of M=5 is expected in DESPEC. From this point of view, the simulation presented here should be a rather accurate representation of reality, since with at most 5 simultaneous photons the chance of more than one detected in the same detector or even in neighbours is not high (especially considering the efficiency of the array). The situation, however, is complicated by the presence of the prompt γ-ray flash due to bremsstrahlung and atomic effects. Depending on the half lives involved and the implantation rate, it may or may not be possible to distinguish such unwanted photons.

Since digitized signals will be available for these detectors, it may be possible to disentangle the prompt flash using timing that is much better than is normally associated with germanium signal shaping time (∼3-6 μs). Since the pulse shape required for position reconstruction lasts for roughly ∼200 ns it may be possible to distinguish between a prompt flash photon followed shortly after by decay photons. Therefore a segment where a bremsstrahlung photon has been detected may still contain a usable pulse shape. If this pulse shape is a net signal, this will come at some expense to the energy resolution[5], for transient signals this need not be a problem. In order to fully account for such effects, a realistic simulation is needed, where among other things, the time structure of the arrival of γ-rays would be included.

Another open question is the realistic gain in possible rate of implantation due to the imaging reconstruction. As described in section 5.2, imaging may be used to distinguish between γ-rays emitted from two or more implanted nuclei present in the detector simultaneously. A cone projection will generally intercept the wafers of AIDA resulting in arcs or circles of possible source locations. The width of these

[5]In this case, two net signals arriving at different times are superimposed in one segment. The determination of their individual energies depends on the time interval between them.

depends on the position resolution given by PSA, however their typical orientation, radius, as well as the distribution of sources in the detector need to be obtained from simulation.

Finally, it should be noted that planar detectors can in principle be arranged in other ways than the box around AIDA as presented in the technical proposal [14] and simulated here. A particular reason to consider other options is that the guard rings of the planar crystals, which present dead volumes of germanium, are occupying the middle of the detector array when placed in a box configuration, where active germanium would otherwise contribute with the highest efficiency.

Appendix A

Digital data acquisition

In order to perform PSA, the signals must be available in a digital form to be processed in a computer or a digital signal processor (DSP). Furthermore, the energy of the pulses must be measured and the trigger condition defined. For the experimental part of this work with the KTH planar detector, a VME-based data acquisition system built by Struck Innovative Systems (SIS) [67] was used. Various data acquisition systems exist and several are being developed for use with segmented detectors. Here the KTH system is described in detail. Similar principles apply to most such systems.

The KTH SIS system consists of up to 8 ADC (analogue-to-digital converter) modules, each equipped with 8 flash ADCs. Here the preamplifier signals are digitized with 14-bit precision at 100 MHz. In other words, the input waveform is converted to discrete values between 0 and 16383 every 10 ns. The dynamic range of the ADCs is 2 V (i.e. the ADC value 16383 is 2 V above the ADC value 0) and can be adjusted between -2 to 0 and 0 to +2 volts. A separate module distributes a clock signal to all ADC modules. It also collects the trigger signals from the individual ADC modules, as well as trigger veto signals, which prevent the creation of a global trigger if any of the modules are, for any reason, not ready. Finally a master module builds events combining the data from the ADC modules and also provides a USB interface to a PC.

The digitized signal arrives at a field programmable gate array (FPGA). Here the signal is passed through two filters, one defining a trigger, the other measuring the energy. Both of these filtered signals are available continuously with a short delay with respect to the raw waveform. There is also a delayed copy of the raw ADC waveform which is sampled when the trigger condition is met, ensuring that the sampled pulses contain data beginning before the trigger was created.

A.1 Moving window deconvolution (MWD)

The input of the sampling ADC system receives a preamplifier signal from a germanium detector. These signals typically have a rise time of 100-200 ns and a much longer exponential decay with a time constant of 50 μs. The energy of a signal is conventionally obtained by an analogue shaping amplifier, where a combination of integrating and differentiating circuits with time constants of a few μs generates a Gaussian, triangular or trapezoidal signal. The amplitude of this signal is sampled and gives the energy deposited in the detector. In a digital sampling acquisition system, an analogous signal processing is done using an MWD algorithm. Since the raw preamplifier signal is continuously sampled, a filter signal, such as the MWD, can be calculated with a short delay relative to the input signal by the FPGA. Fig A.1 illustrates a result of an MWD filtering on a preamplifier signal. A trapezoidal signal is created when a difference is taken between sums of the signal in two moving windows (whose lengths correspond to the rising and falling edges of the trapezoid) separated by a time corresponding to the length of the top of the trapezoid.

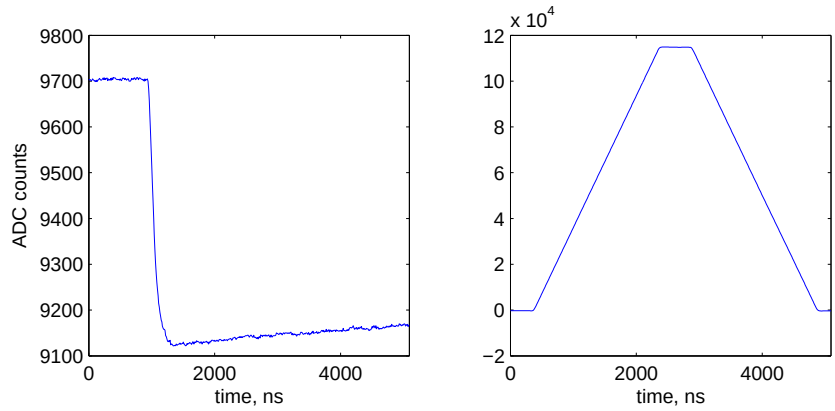

Figure A.1: A raw preamplifier pulse (left) and its moving window deconvolution (right).

Let R_k be a sample of the raw preamplifier signal, P – the peaking time (number of samples over which the summation occurs) and G – the gap time (the number of samples between the two moving windows). Assuming that the input signal is a step function, a sample of the MWD signal, M_i is given by

$$M_i = -\sum_{k=i}^{i+P-1} R_k + \sum_{k=i+P+G-1}^{i+2P+G-2} R_k \tag{A.1}$$

Realistic preamplifier signals, however, have an exponential decay, whose time constant is usually around τ=50 μs. With the definition in the equation A.1, the resulting MWD signal will not return to a zero baseline. A decay correction can be added as follows.

$$M_i = -\sum_{k=i}^{i+P-1} R_k + \sum_{k=i+P+G-1}^{i+2P+G-2} R_k + \frac{P}{\tau} \sum_{k=i}^{i+P+G-1} R_k \tag{A.2}$$

Equivalently, the algorithm can be defined as a differentiation with the time constant P $(R_{i+P} - R_i)$ followed by a running average over $P + G$ samples. In this case the first step results in an approximately rectangular signal and the second creates the trapezoid. This method is employed in the work of M. Lauer [68], where the implementation of MWD is described in more detail. In practice a recursive definition is used to avoid the need for summation in each step:

$$M_{i+1} = M_i + R_i - R_{i+P} - R_{i+P+G-1} + R_{i+2P+G-1} - \frac{P}{\tau} R_i + \frac{P}{\tau} R_{i+P+G} \tag{A.3}$$

The effect of the decay correction is similar to that of the pole/zero cancellation in an analogue amplifier. It is of a particular importance in situations with high signal rates since an inadequate correction will result in signals residing on a baseline that may be shifted after a previous pulse. This is illustrated in fig A.2. In this example, two photons of equal energy are absorbed in the detector 20 μs after each other. While the two preamplifier pulses have a significant overlap, the deconvolved signal shows two well-separated peaks. However when no decay correction is used, the amplitudes are substantially different.

The energy value can be defined in a number of ways, and several methods have been implemented in the KTH SIS system. It is for instance possible to sample the baseline before the trapezoid and at the top of the trapezoid at predefined sample indices. Alternatively maximum and minimum values can be used. In fig. A.2, MWD data is sampled at the maximum and the sample before the trapezoid starts. The samples chosen are indicated with an asterisk.

A.2 Trigger generation and sampling modes

In addition to the energy filter described above, each channel of the system also has a much faster trapezoidal filter used to define the trigger. This filter uses much smaller parameters P and G (on the order of 100 ns)[1] in order to provide a trigger with only a short delay after the start of the signal. This operation is similar to a timing filtering amplifier (TFA) in analogue systems. The fast filter signal is compared to a threshold, defining a trigger for the particular channel. The

[1]Shorter integration results in better timing, on the other hand a longer peaking time is favourable in situations with high noise or low threshold.

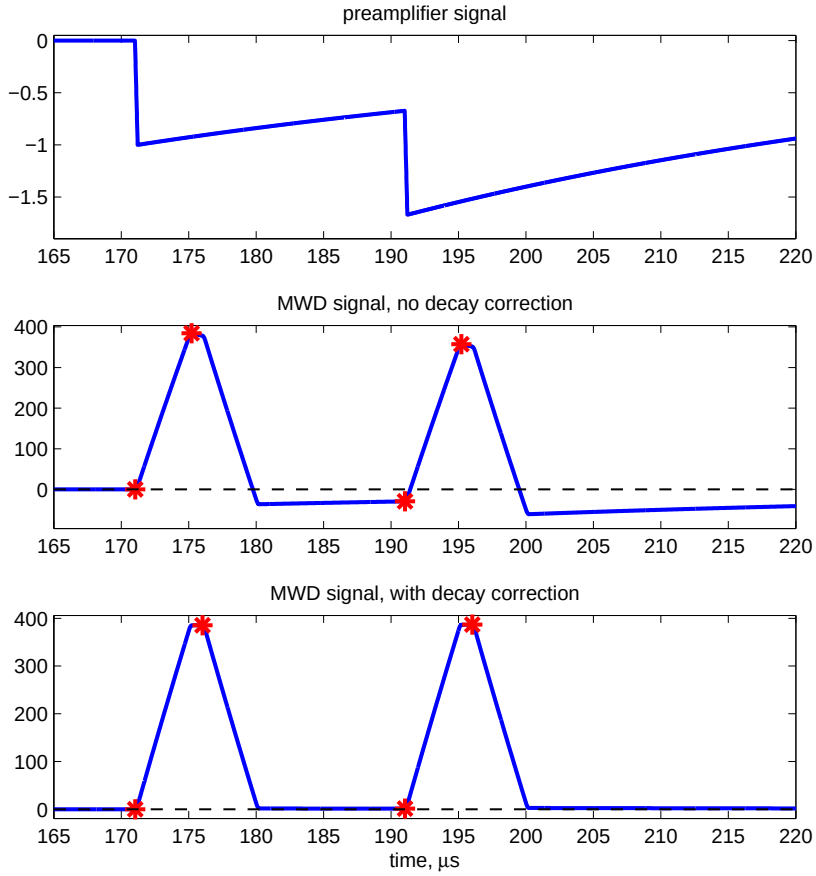

Figure A.2: *Top:* preamplifier pulse corresponding to two γ-rays of equal energy with the delay of 20 μs. The amplitude of each pulse is set to 1. *Middle and bottom:* MWD without and with a decay correction. In this case, assuming the γ-ray energy of 1332 keV, the energy measured for the second pulse with no τ correction has an error of 8 keV and only 0.4 keV with the correction. Here, P=400 samples =4 μs (hence the amplitude of the trapezoid of $\approx$400 ADC units) and G=100 samples =1 μs.

trigger signals from all channels (for which the trigger output is enabled) are sent to the clock module where a decision is made on whether a global trigger should be created or not. Alternatively, an external trigger signal can be used. When a trigger condition is fulfilled, delayed preamplifier signals are sampled in order to provide waveforms that begins before the event has occurred.

There are three main sampling modes available in the current implementation of the KTH SIS system. In each case, the computer controls the retrieval of data.

Single event synchronous mode: all channels in modules that are enabled are sampled simultaneously and the event is sent to the computer immediately. This operation mode can be used in a fashion similar to an oscilloscope – in order to quickly assess the state of the system, visualise the detector signals or adjust the decay correction. The maximum rate is, however, limited to only a few 10 Hz due to large latencies in the transfer of data that occurs after each event. This mode can also be used when collecting very rare events, for example during a detector scan when a weak source or very narrow collimators are used.

Multiple event synchronous mode: similar to the single event mode, however events are stored in the memory of the master module and only transferred to the computer once this memory is full (or when a maximum number of events is exceeded). Depending on the amount of data stored per event, rates of a few 10 kHz can be handled. A disadvantage is the period of dead time during the transfer of the data (up to 128 MB). This is the main data acquisition mode used for segmented detectors.

Multiple event asynchronous mode: In this case, each ADC module collects data from its own 8 channels and stores it in a local memory. Only data from a channel that triggered is saved. The computer periodically retrieves all events from each module. Since the event size is much smaller and the full system does not suffer dead time when one of the modules triggers, a rate of 100 kHz and above can be reached. Events are not stored chronologically, but in the order the module buffers were retrieved and can later be correlated using the event time stamp. This mode was used for energy calibration when coincident pulse shape information is unnecessary.

Acknowledgements

Allow me a few lines to thanks the following. Bo Cederwall for the opportunity to partake in the endeavours chronicled herein, and no less for encouragement and aid in participation in numerous confluences and assemblages of people of wisdom and experience; as too a number of experimental undertakings in great halls of many wondrous contraptions. The value of such convergences cannot be overlooked, for do so, would be to undermine their contribution to the breadth and an invigorating sense of purpose in the undertakings of my own. Arne Johnson, for thorough study and opinions of this manuscript and discussions of matters of consequence and otherwise with great scope in time and application. Torbjörn Bäck has also glanced upon these pages and shared such wisdom as to improve them; and too, has championed the struggle against all entities – mystic and mundane – that reside in voids between contraptions, storages of memory and things with buttons. Lars-Olov Norlin for many times of valiant aid within the lower levels of the building, where few others venture, for here is filled with curious contraptions; and no less, for tales of many great exploits of the past.

I wish to thank my forerunner, Larissa Milechina, whose writings were an inspiration, wisdom and guidance in early days of my endeavours. Further notable thanks to Stanislav Tashenov who facilitated my acquaintance with HISPEC and DESPEC; for his immeasurable enthusiasm concerning matters of science and scientific contraption and the mixtures of the two in any proportion; and without whom such adventures as the expedition into the town of Darmstadt would never have occurred. For the companionship in the latter, so too must Kai-Uwe Schässburger be thanked. Alas, more names will be omitted for the sake of such brevity as can be salvaged, nevertheless, remembered are those others of the group who shared these wall the years past.

Many scientists encountered in various conferences have had an important influence upon my work. Here, only few can be acknowledged in particular: A. Gadea and A. Jungclaus for enthusiastic discussion and suggestions; A. Algora for casting the dice and thereby predicting the interaction of photon and contraption; and others of HISPEC/DESPEC collaboration. Those in AGATA collaboration, for many convergences abounding with enlightenment and cuisine. A. Boston, H. Boston, R. Cooper, C. Unsworth and others in Liverpool for help with data from Smart-PET, and similarly G. Hackman and S. Williams for kindly transmitting TIGRESS

data.

At last, I wish to raise the goblet and say a cheer to our fellows – Janne, Mikael, Merja and other neutrons – for their lively spirit and great comradery in volumous consumption of brews known as *coffee* and meats known as *cake* and all those others whom I am proud to know as friends and relatives – those too, who may not hail from circles of the nuclear.

Bibliography

[1] L. Milechina, *Development of gamma-ray tracking algorithms and pulse shape analysis methods for highly segmented ge detectors*, PhD thesis, KTH, Stockholm, 2004.

[2] K. Vetter et al., Nucl. Instr. Meth A452 (2000) 223.

[3] AGATA technical proposal (2001)
http://www-w2k.gsi.de/agata/Agata_pub-proposal.pdf

[4] XCOM: Photon Cross Sections Database (2007)
http://physics.nist.gov/PhysRefData/Xcom/Text/XCOM.html

[5] K.-U. Schässburger, *Si-Detector Development for γ- and X-ray Imaging Applications*, master's thesis, KTH, Stockholm, 2008.

[6] J. Eberth, et al., Prog. Nucl. Part. Phys. 28 (1992) 495.

[7] http://www.phys.jyu.fi/research/gamma/jurogam/

[8] H.J. Wollersheim et al., Nucl. Instr. Meth. A537 (2005) 637.

[9] E. Azaiez, Nucl. Phys. A654 (1999) 1003.

[10] J. Eberth, et al., Prog. Nucl. Part. Phys. 46 (2001) 389.

[11] C. E. Svensson et al., J. Phys. G: Nucl. Part. Phys. 31 (2005) 1663.

[12] J. Simpson, J. Phys. G: Nucl. Part. Phys. 31 (2005) 1801.

[13] I. Y. Lee, et al., Proc. of Conf. RNB6, Nucl. Phys. A 746 (2004) 255.

[14] HISPEC/DESPEC technical proposal (2004)
http://personal.ph.surrey.ac.uk/∼phs1zp/Tech_Proposal_HISPEC_DESPEC-28-01.pdf

[15] F. Recchia, et al., Nucl. Instr. Meth. A604 (2009) 555.

[16] A. Gadea, et al., LNL Annual Report 2008, p39. http://www.lnl.infn.it
/∼annrep/read_ar/2008/contributions/pdf_singles/39.pdf

[17] J. M. Ryan, Nucl. Phys. B (Proc. Suppl.) 10B (1989) 121.

[18] T. Niedermayr, et al., Nucl. Instr. Meth. A553 (2005), 501.

[19] H. C. Boston, et. al., Nucl. Instr. and Meth. A580 (2007), 929.

[20] R. J. Cooper, et al., Nucl. Instr. and Meth. A579 (2007), 313.

[21] K. Vetter, et.al., Nucl. Instr. and Meth. A579 (2007), 363.

[22] J. Eberth and J. Simpson, Prog. Part. Nucl. Phys. 60 (2008) 283.

[23] R. M. Keyser, T. W. Raudorf, Nucl. Instr. Meth A286 (1990) 357.

[24] D. Protic, T. Krings, IEEE Trans. on Nucl. Science 51, NO. 3 (2004) 1129.

[25] R. J. Dinger, IEEE Trans. on Nucl. Sience 22 (1975) 135.

[26] H. L. Malm, R. J. Dinger, IEEE Trans. on Nucl. Science 23, NO. 1 (1976) 76.

[27] W. L. Hansen et al., IEEE Trans. on Nucl. Sciencc 27 (1980) 247.

[28] J. Llacer, H. W. Kraner, Nucl. Instr. Meth 9c (1972) 467.

[29] L. Mihailescu et al., Nucl. Instr. Meth A44c (2000) 350.

[30] B. Bruyneel et al., Nucl. Instr. Meth A569 (2006) 764.

[31] L. Milechina, B. Cederwall, Nucl. Instr. Meth A55 (2005) 278.

[32] R.J. Cooper, *Performance of the SmartPET Positron Emission Tomography System for Small Animal Imaging*, PhD thesis, University of Liverpool, 2007.

[33] http://www.comsol.com

[34] A. Shockley, J. Appl. Phys. 9 (1938) 635.

[35] S. Ramo, Proc. IRE 27, (1939) 584.

[36] L. A. Hamel, M. Julien, Proc. SPIE vol. 4507 (2001) 255.

[37] L. A. Hamel, M. Julien, Nucl. Instr. Meth A597 (2008) 207.

[38] L. Nelson et al., Nucl. Instr. Meth A573 (2007) 153.

[39] I. Kojouharov et.al., NSS '07. IEEE, vol. 3 (2007) 2213.

[40] F. C. L. Crespi et al., NSS '08 IEEE (2008) 3237.

[41] Th. Kröll, D Bazzacco, Instr. and Meth. A 565 (2006) 691.

[42] A. Olariu et al., IEEE Trans. on Nucl. Science 53, NO. 3 (2006) 1028.

[43] *Solving Least Square Problems*, C.L. Lawson and R.J. Hanson, SIAM (1995).

[44] http://www.mathworks.com

[45] F. C. L. Crespi et al., Nucl. Instr. Meth A570 (2007) 459.

[46] A.J. Boston et al., Nucl. Instr. Meth B261 (2007) 1098.

[47] T. Habermann, *Optimierung des elektrischen Feldes in planaren Germanium Pixeldetektoren*, Master's thesis, GSI, Germany, 2007.

[48] B. Bruyneel el al, Nucl. Instr. Meth A599 (2009) 196.

[49] B. Bruyneel el al, Nucl. Instr. Meth A608 (2009) 99.

[50] B. Bruyneel el al, Nucl. Instr. Meth A569 (2006) 774.

[51] J.D. Kurfess et al., Nucl. Instr. Meth A505 (2003) 256.

[52] D. Brusa, et al., Nucl. Instr. Meth. A379 (1996) 167.

[53] F. Persson, *Simulations and analysis of Compton camera configurations*, ISSN 0280-316X, Master's thesis, KTH, Stockholm, 2008.

[54] R.M. Kippen, New Astr. Rev.48 (2004) 221.

[55] S. Tashenov, *Hard x-ray polarimetry with position sensitive germanium detectors – studies of the recombination transitions into highly charged ions*, PhD thesis, GSI, Germany, 2005, urn:nbn:de:hebis:30-48631 (http://publikationen.ub.uni-frankfurt.de/volltexte/2007/4863/).

[56] A. Ferguson, Nucl. Instr. Meth. 162 (1979) 565.

[57] S. Tashenov et al., PRL 97 223202 (2006).

[58] H. Geissen et al., Instr. and Meth. B204 (203) 71.

[59] K.-Th. Brinkmann et al., Nucl. Phys. A 790 (2007) 75c.

[60] M. Sandzelius et al, PRL 99, 022501 (2007).

[61] Z. Podolyak, Nucl. Instr. and Meth. B226 (2008) 4589.

[62] L. Caceres et al., Phys. Rev. C 79, 011301(R) (2009)

[63] S. Tashenov, J. Gerl, Nucl. Instr. and Meth. A586 (2008) 224.

[64] www.cern.ch/geant4/

[65] F. Recchia, et al., Nucl. Instr. Meth. A604 (2009) 60.

[66] P. Detistov et al., Acta Phys. Polonica B Vol. 38 (2007) No 4, 1287.

[67] Struck Innovative Systems
http://www.struck.de

[68] M. Lauer, *Digital Signal Processing for segmented HPGe Detectors Preprocessing Algorithms and Pulse Shape Analysis*, PhD thesis, 2004.